Fast electron tomography: Applications to beam sensitive samples and in situ TEM or operando environmental TEM studies

Siddardha Koneti, Lucian Roiban, Florent Dalmas, Cyril Langlois, Anne-Sophie Gay, Amandine Cabiac, Thomas Grenier, Hussein Banjak, Voichita Maxim, Thierry Epicier

To cite this version:

Siddardha Koneti, Lucian Roiban, Florent Dalmas, Cyril Langlois, Anne-Sophie Gay, et al.. Fast electron tomography: Applications to beam sensitive samples and in situ TEM or operando environmental TEM studies. Materials Characterization, 2019, 151, pp.480-495. 10.1016/j.matchar.2019.02.009 . hal-02151235

Version of Record: https://www.sciencedirect.com/science/article/pii/S1044580318330286
Manuscript_e62339f40ea5e2f63347ea9eb55578c9

Fast electron tomography: applications to beam sensitive samples and in situ TEM or operando Environmental TEM studies

Siddardha Koneti[1], Lucian Roiban[1*], Florent Dalmas[1], Cyril Langlois[1],
Anne-Sophie Gay[2], Amandine Cabiac[2], Thomas Grenier[3], Hussein Banjak[3],
Voichiţa Maxim[3], Thierry Epicier[1*]

[1]*Univ Lyon, INSA-Lyon, Université Claude Bernard Lyon 1, MATEIS, UMR 5510, CNRS, 69621 Villeurbanne Cedex, France*

[2] *IFP Energies nouvelles – Rond-point de l'échangeur de Solaize, BP 3-69360 Solaize, France*

[3] *Univ Lyon, INSA-Lyon, Université Claude Bernard Lyon 1, CREATIS, CNRS UMR 5220 – INSERM U1044, 69621 Villeurbanne Cedex, France*

Abstract:

Electron Tomography (ET) is of greatest interest in studying nano- and biological materials since it gives access to 3D morphological, chemical and physical features. Even though ET techniques have been continuously improved in the last decades, they are still limited: lengthy time scales (tens of minutes) are generally needed for the tilt series acquisition prior to the volume reconstruction step. Such long exposures to a relatively intense electron beam lead to large electron doses received by the sample. This may promote extensive irradiation damage in the case of soft materials like polymers and bio-materials when they are not protected through dedicated sample preparation methods, and any tomographic reconstruction will then be meaningless. More importantly, the time constraints drastically limit 3D investigations during dynamic *in-situ* experiments where the sample rapidly evolves during the acquisition.

We present here developments for acquiring tilt series of projections in very short time scales, readily down to a few seconds. After an outlook of possible ways to speed up the data acquisition in the bright field imaging mode (BF-TEM), strategies for the fastest methods in 'step-by-step' and 'continuous tilt' ET will be described. Applications of these procedures are presented on various systems, including metallic Pd nanoparticles deposited on alumina, and soft materials like polymer nanocomposites and biological matter. A special reference is made to fast operando nano-tomography performed on nanomaterials during their dynamic evolution. The feasibility of fast ET is exemplified by a calcination study of Pd catalysts supported by SiO_2 at 400°C and 500°C under 4 mbar H_2 in a dedicated Environmental Transmission Electron Microscope (ETEM).

*corresponding authors.

Corresponding authors:

Thierry EPICIER

thierry.epicier@insa-lyon.fr. Tel.: +33(0)687883069; FAX: +33(0)472438830.

Lucian ROIBAN

Lucian.roiban@insa-lyon.fr. Tel.: +33(0)472436131; FAX: +33(0)472438830.

Keywords:

Fast operando Electron Tomography; nanocatalysts; Environmental Transmission Electron Microscopy (ETEM); Pd-Al_2O_3; Pd-SiO_2.

Highlights:

- Fast image acquisition for Electron Tomography (ET) can take only a few seconds
- A continuous rotation of the sample allows relevant and fast acquisition for ET
- Fast ET is possible under gas and temperature conditions *in-situ* in a ETEM
- Repeated acquisitions on the same object allow to follow its evolution in operando
- The resistance to sintering of Pd@SiO_2 nanocatalyst is quantified in situ in 3D

Graphical abstract:

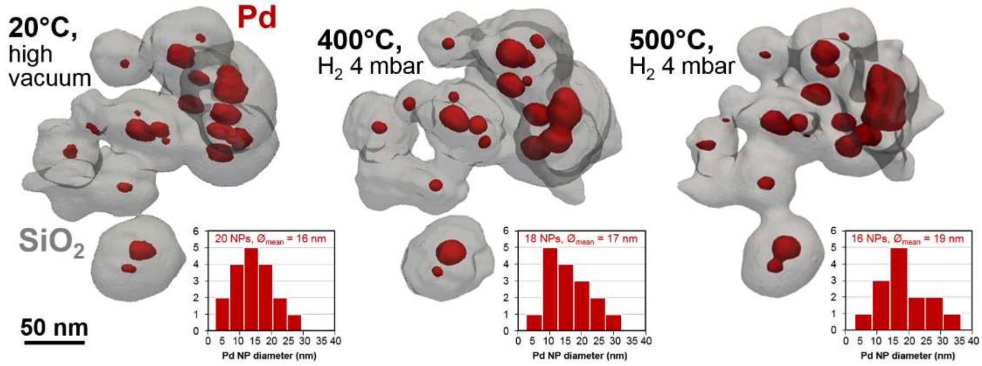

Competing interest statement:

the authors have no competing interests to declare.

1. Introduction

1.1. Context of the study: brief overview of Electron Tomography approaches in a TEM

Transmission Electron Microscopy (TEM) is an unsurpassed technique to characterize materials at a micro, nano and sub-nano scale [1]. Recent technical developments contribute to provide newer information with higher accuracy. Among the imaging techniques, Electron Tomography [2,3] (ET) has become a robust and reliable approach to obtain quantitative information on three-dimensional structural and morphological features of nanomaterials at nanometric [4,5] and even atomic resolution [5,6,7]. ET consists in acquiring series of projections from the object in different orientations over a large angular amplitude, so-called tilt series. Then, specific reconstruction algorithms [8,9,10,11] implemented in different softwares [12,13,14,15,16,17,18,19] are used to retrieve the 3D nanoscale structure of the material. The consistency of the reconstruction relies on the projection approximation which establishes an unambiguous and linear relationship between the image intensity and the mass-thickness of the sample [20]. This criterium may not be completely fulfilled in Bright Field -TEM (BF-TEM) because of diffraction contrast. However, this is not a limitation in the case of non-crystalline objects. As an example, biological matter has been studied in BF-ET since many decades [21,22,23] and is still currently investigated especially in the cryo-EM mode [22,24]. Poorly-crystalline samples exhibiting moderate diffraction contrast, like nanocatalysts [25], hybrid or mesoporous materials [4] can also be reasonably studied this way. For thicker and highly crystalline materials, BF-TEM may hamper representative 3D reconstructions and more incoherent imaging or analytical modes such as STEM-HAADF (Scanning Transmission Electron Microscopy, High Angle Annular Dark Field imaging) [5,23,26,27], Energy-Filtered TEM (EFTEM) [4] or scanning mode STEM-EELS [28] (STEM coupled with Electron Energy-Loss Spectroscopy) and STEM-EDX (STEM coupled with an energy-dispersive X-ray spectrometer) [29,30] are thus preferred to limit undesirable diffraction effects. Among these approaches, STEM-HAADF is typically the most widely employed. Today, several commercial and home-made softwares and/or plugins are available for ET acquisition with modules driving the mechanical rotation of the TEM goniometer. They are able to perform object tracking between successive images (by adjusting the beam shifts), to correct the focus (through changes of the objective lens excitation using pairs of beam tilted images) and record the image by controlling the camera [17,18,19,31,32,33,34,35,36]. Depending upon the degree of sophistication of the routine used, acquiring the tilt series includes several steps:

(i) Step-by-step rotation of the object between successive tilts, using equal or Saxton [37] tilt increment or controled dose tilt-scheme [38]

ii) Calculation of cross-correlation (or equivalent) operations or manual intervention of the user to track the object and keep it in the field of view

(iii) Optional adjustment of the focusing conditions (either manual or automated)

(iv) Acquiring and saving each image with the value of its corresponding tilt angle.

All those steps cost computing time during which the sample is exposed to the electron beam which may favour irradiation damage and increases the total duration of the step-by-step tilt series acquisition. Typically, the adequate amplitude of tilt is between +70° and -70° with dedicated tomographic sample-holders and the angular step is set to one or two degrees. For such conditions, the total acquisition time for a tilt series is of the order of tens of minutes in BF mode, one or two hours in STEM mode and even more for analytical modes such as EFTEM and STEM-EDX. These significant differences are due to the image acquisition time, of the order of a fraction of second in Bright Field, but several seconds up to a few minutes in all other imaging modes. The time needed to record an image is due to the scan procedure in STEM and/or to the low signal-to-noise ratio requiring long exposure times in STEM-EDX and EFTEM modes. In all cases, ET is consequently mainly applicable for 3D characterization of nanomaterials that do not suffer from irradiation damage due to a large cumulative electron dose during a long exposure time. Beam sensitive samples such as biological material, organic, carbonaceous, hybrid and mesoporous materials are thus generally analyzed in 3D using specific approaches such as low dose or cryo techniques [39]. Indeed, the degradation possibly caused by the electron beam to the object remains a concern especially in the case of soft matter: any significant morphological change of the sample during the ET acquisition will obviously prevent from correct volume reconstruction. When the duration of the ET acquisition is an issue regarding irradiation, it is also a severe obstacle for following the 3D evolution of nanomaterials under dynamic *in-situ* conditions. This constraint is common to micro- and nano Computed Tomography in X-ray approaches at synchrotron; these aspects are more specifically detailed in the next sub-section 1.2.

1.2. 3D experiments in environmental TEM

A typical situation where nanomaterials are studied under *in-situ* conditions concerns Environmental Transmission Electron Microscopy (ETEM), where gas and/or liquid are inserted around the sample. In addition, the sample can be heated in order to study chemical, structural and morphological transformations. We are mainly interested here with environmental microscopy performed in a dedicated ETEM, where a differential pumping system transforms the pole-pieces space into an environmental chamber in the column of the microscope (see for example [40,41,42]). ETEM has been the subject of considerable developments and exciting applications during the last decades, owing to the availability of technologically advanced instruments. It is beyond the scope of this work to review such developments, but it is worth mentioning that ETEM allows to follow the dynamics of gas-solid interactions, gas-driven transformations and chemical reactions, such as adsorption of molecules on surfaces, growth of carbon nanotubes, oxidation or reduction process even at atomic resolution [43,44,45,46]. According to these developments, one may wonder whether 3D characterization of such nanomaterials can be performed *in-situ* by ET in order to follow their evolution under environmental conditions. Clearly, as stated above, the main issue is the long time needed for recording the ET tilt series with respect to the kinetics of the chemical or morphological transformation that is studied. Because it is of the highest interest to characterize such evolutions on nanomaterials in 3D, few conventional ET experiments have already been performed *post-mortem* 'before' and 'after' *ex-situ* environmental solicitation in an external cell or reactor [47,48,49,50]. Such a strategy is very delicate, since it requires to insert, retract and re-insert the sample in and out of the microscope several times. Furthermore, it does not offer suitable conditions to follow the 3D transformation dynamically.

The purpose of the present paper is to state upon the possibilities of accelerating tilt series acquisition in the Bright Field mode allowing to track a dynamic 3D transformation using dedicated ETEM. At the same time, the application of fast ET to beam sensitive samples will be illustrated.

To the best of our knowledge, the only and first work devoted to an in situ 3D characterization successfully performed under environmental conditions in an ETEM is the recent study of the calcination of an Ag@silicalite-1 with possible applications for selective catalysis [51]. In this example, coalescence and disappearance of Ag nanoparticles encaged in hollow silicalite-1 occurred in a few minutes according to the slow reactive conditions dictated by the low O_2 partial pressure at 280 °C and 450 °C. Tomograms of the same area of interest were reconstructed using tilt series recorded in 2 minutes each at 20 °C in vacuum, at 280 °C and 450 °C under 1.8 mbar of O_2. This allowed the computing of the tomographic volume of the same group of objects at different temperatures, while keeping the electron dose below a minimum where no significant irradiation damage was detected. Whereas this is still a challenge in TEM, second or sub-second temporal resolution has been achieved at synchrotron facilities since less than a decade, owing to the high flux and high sensitivity detectors that allow performing 180° tilting series acquisition at a very high rate. Recent works allowed tomographic acquisitions to be performed at a frequency of several Hz in both life sciences (e.g. biomedical applications as study of cardiac [53] or respiratory systems [54]) and materials science [55] (e.g. mechanical testing of alloys or heat treatments). Approaching these performances is thus a motivation to investigate the possible ways to reduce the acquisition time in ET down to the second range. This objective restricts us today to the usual bright field TEM imaging mode. It should obviously be kept in mind that the question of a compromise between time and resolution will have to be considered.

2. Current technical possibilities for fast electron tomography

2.1. Brief survey of technical approaches

The typical duration of a tilt series acquisition is of several minutes. We review hereafter some of the solutions that have been proposed to reduce this recording time.

The first one is to use a limited number of projections of the sample and to reconstruct the volume by adequate algorithms like the discrete tomography technique [10,56]. The main potential of this approach seems to be in the 3D characterization of monocrystalline nanoparticles at atomic resolution in STEM mode [57,58]. Although this technique allows in principle to speed up the acquisition, the objective to realize it in less than one minute has not been reached yet.

As mentioned above, stopping the rotation of the sample at each angular position is also time consuming. From then, a natural idea and second solution is to speed up the sample rotation procedure by tilting the goniometer continuously instead of using the classical step-by-step procedure, and acquire images continuously during this movement. Note that in some very rare situations, one can take profit of the free rotation of the sample itself, as it was pertinently performed in the case of a nanoparticle in a liquid cell [59]. This continuous rotation of the sample has been already used in electron diffraction tomography [60,61], where the acquisition typically takes a few minutes. It has also been employed in structural biology [62], and in a specific study of a lanthanide-based inorganic nanotube [63]. The substantial gain of time generated by continuous rotation comes at the cost of the impossibility to perform, for now, any live tracking of the object. Another disadvantage might be a limited signal-to-noise ratio of the images as compared to the step-by-step rotation, beacause the exposure times must be short enough to avoid any significant drift of the object during the image acquisition. A long exposure time of the camera while continuous rotation of the object will lead to crippling blurring of the recorded projections. At this stage, it appears convenient to record the tilt series continuously at a very high rate, and very short exposure times (constituting them a series of moving images that we can commonly name a video sequence), instead of as single snapshots [51,63,64].

A third solution became recently possible owing to the availability of fast and sensitive optimized-CMOS and/or Direct Electron detection cameras (DE) since roughly the beginning of the XXIst century. Currently, digital cameras use a scintillator to convert electrons into photons. DE devices detect directly the incoming electrons offering thus a much better sensitivity, signal-to-noise ratio and resolution [65]. Such devices are available today from several manufacturers: Falcon^{TM} series from FEI [66,67], K2^{TM} [68] and more recently K3^{TM} [69] from Gatan, DE^{TM} series from Direct Electron [70], pn-CCDs from PNSensor [71]. Owing to their high sensitivity, they allow acquiring images in miliseconds depending upon their binning capabilities. With slightly lower performances, optimized CMOS-based cameras of the lastest generation like Ceta^{TM} from FEI [72], Oneview^{TM} from Gatan

[73] or TemCam XF^{TM} series from TVIPS [74] still allow acquisitions of 25 to 50 frames per second (fps) in 4k x 4k format. The combination of the two latest solutions, i.e. recording a video sequence using a high-speed camera during a continuous rotation was tested on a carbon nanotube at room temperature and in high vacuum [63], where a tilt series over an angular range of 100° was performed in less than 4 seconds. Very interesting approaches are also currently developed in the perspective of real-time 3D *in-situ* straining experiments [75], where the total acquisition time is of the order of 2-3 minutes over 120° rotation amplitude. Using a straining holder [76] it is possible to record several tilt series during a straining experiment and follow the deformation of the sample in 3D.

From the above, a promising solution for performing fast tomography consists in recording the tilt series during a continuous rotation of the object with a high speed recording camera. Before detailing experimental results, we will stress out some of the limitations of this approach.

2.2. Optimized 'step-by-step' acquisition versus continuous rotation approach

Figure 1 sketches the difference between the step-by-step acquisition, where the sample is tilted with a given angular increment between successive images, and the continuous rotation technique, leading to a much smaller angular increment.

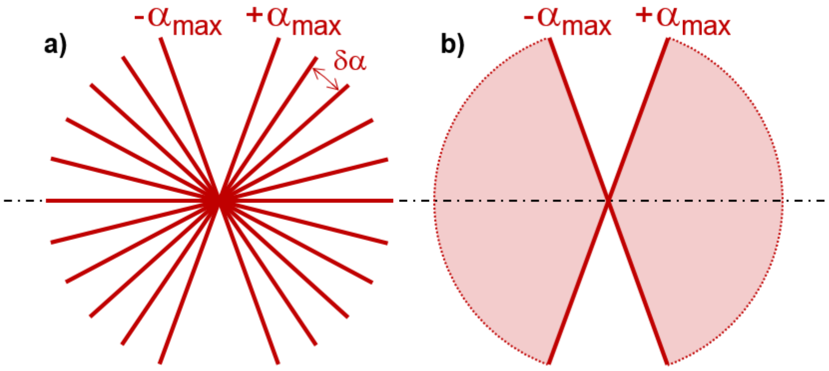

Figure 1: Tomographic acquisition in the angular range [$-\alpha_{max}$, $+\alpha_{max}$], with α_{max} typically equal to +70° . a) Conventional step-by-step electron tomography with a pre-defined angular step $\delta\alpha$ (2° typically). b) Continuous rotation of the sample leading to a much smaller angular increment depending on the rotation speed (schematic). ***1-column figure.***

The step-by-step procedure (called SBSET for Step-By-Step Electron Tomography hereafter) can be speeded up by allowing human intervention. As already mentioned in the first section of this work, most of the computer-driven tilt series acquisition routines slow down the process because of adjustments between successive images, e.g.. tracking and focusing. These corrections can be done manually assuming that the rotation procedure remains relatively low. This also implies that the initial adjustment in z of the sample on the tilt axis (adjustment of the eucentric height) is fine enough to limit the shift of the area of interest in the field of view during the rotation. Table 1 gives typical durations for recording tilt series composed of 2k x 2k images. The angles are sampled every 2° between +70° and -70° and the images are acquired either with a conventional digital camera (such as a CCD-based camera) or with a fast recording camera of the latest generation. The times per frame are experimental values for an acquisition using either a fully automatic, with software-based corrections (conventional mode), or a semi-automatic (fast mode) procedure. The time gain in the latter case is due to the reduction of the adjustment time needed after tilting before recording the image at the respective angle. This time includes a relaxation time needed for the goniometer to stabilize and the time required for adjustements such as centring the object within the field of view or correcting any possible defocus. While a software is successively calculating the position and the focus of the sample in about 45 s, an experienced user can do it faster, even close to 1 s. Although, it may be user and experiment-dependent, the manual step-by-step procedure offers the possibility of an acquisition in less than 3 or even 2 minutes.

Experimental procedure	**Software-based acquisition**		**Semi-automatic acquisition**	
	Conventional digital camera	*Optimized CMOS or DE camera*	*Conventional digital camera*	*Optimized CMOS or DE camera*
Acquisition time for one 2k x 2k image (s)	0.2	0.01	0.2	0.01
Angular increment between images (°)	2			
Time for tilting between two successive angles (s)	0.1			
Total number of images	71			
Adjustment time needed after tilting (s)	45		1	
Total acquisition time	52 min 51 sec	52 min 38 sec	1 min 31 sec	1 min 18 sec

Table 1: Recording times for a +70 to -70° SBSET tilt series. For a fully automatic software-based acquisition, the time was estimated using the FEI tomography plugin; for the semi-automatic acquisition, the time was estimated using a home-made plugin [51]. For both methods, we considered the exposure time needed for the camera to record an image having a reasonable signal-to-noise ratio. To calculate the total time needed to record a tilt series, we considered an angular increment of 2°, the time needed to tilt the sample from one angle to the next and some adjustment time at each angle.

The semi-automatic approach remains unfortunately still too slow to follow fast dynamic events, mainly because of the time required for keeping the object in the field of view and possibly re-adjusting the focus. To reach this objective, we propose to avoid any stop during the rotation, and to continuously rotate the sample while the camera records the images at a rate as high as possible. In these conditions, focus variations and some systematic blur effect produced by the rotation of the object during recording may be an issue, even with very short exposures on DE-type high-speed cameras. These aspects are discussed hereafter.

2.3. Possible blur sources during CRRET

While continously rotating the sample and recording images, three different types of inescapable blur can affect the quality of a tomography experiment performed with the Continuous Rotation and Recording approach (labeled hereafter as CRRET for Continuous Rotation and Recording Electron Tomography). It is not the purpose of the present paper to analyze thoroughly the different possible sources of blur, however we can summarize them as follows (see also Figures SM1 and SM2 in Supplementary Material - SM -):

(i) Random (x,y) (and z related to focus) shifts of the sample

They are due to mechanical instabilities of the goniometer while rotating or to a bad eucentric alignment, and induce motion blur in the images recorded with a long exposer time reported to the speed of these movements.

(ii) High frequency vibrations at high rotation speed of the goniometer.

The goniometers were certainly conceived to stably sustain the sample and to move it slowly in order to preserve the high resolution imaging. However, most of current systems were probably not designed for fast tilting. Such vibrations are perceived at relatively high speed rotation of the goniometer.

(iii) The ‘rotational blur’ summed up during the acquisition of each image

as a consequence of the compromise between the rotation speed and the exposure time of the camera.

Drifts along the z direction produce an out-of-focusing of the sample which is not necessarily very severe in the BF mode owing to its large depth-of-focus in nearly parallel illumination. In addition, Fresnel diffraction contributing to the z-blur effects are minimized in an image obtained with a microscope equipped with a Cs-corrector such as the one used in this study (sections 3 and 4). In the very best cases, the eucentric alignment is sufficiently good to simultaneously keep the object in the field of view and in acceptable good focus and no correction during the acquisition is needed. Such an example is shown in the operando fast tomography experiment on a Pd-SiO_2 catalytic system presented hereafter (section 4.3).

The vibration blur (ii) will not been discussed here because it can not be counteracted by the user so far. Further improvements have to be made by the manufacturers to address these instabilities which affect most of the projections.

We will now have a deeper look at the third point about the rotational blur. To evaluate its influence on the final tomographic image, we run simulations as illustrated by Figure 2. From a previous study [51] we have selected a classical BF 2D image playing the role of a 2D phantom as commonly used in other studies [77,78,79]. This micrograph shows a nano-catalyst system made of Ag nanoparticles having an average size of 6 nm encaged in silicalite-1, e.g. a zeolite-type mesoporous silica [80]. This reference phantom was then rotated numerically between -70° to 70° with an angular step of 0.1°. To mimic the blur that a rotation θ integrates in a projection recorded during a certain exposure time, an adequate number of 'elementary' phantoms rotated every 0.1° were averaged and their 1D projections were calculated using a home made software. For example, 1D projections with a 1° rotation blur were calculated from a 2D phantom made by averaging 10 'elementary' phantoms. Respectively, 20 such 'elementary' phantoms were used for a 2° rotation blur, and 100 ones for the 10° rotation blur, as illustrated in the series of objects all shown at zero tilt in Figure 2a).The 0°-rotation phantom is sharp and unblurred: the Ag nanoparticles appear as dark dots, and the walls of the silicalite-1 container are well defined.

For the reference phantom (0°) as well as for the integrated blured phantoms, the 1D projections along the vertical direction are calculated. Their intensity profile is plotted (Figure 2b) and the signal becomes smoother as the rotation blur increases from 0° to 10°. Note that a more complete version of this figure including sinograms is reported in SM as Figure SM2.

Figure 3 shows the 2D-reconstructions calculated from 1D projections having various integrated blur conditions. These blur conditions can be subsequently translated into speed rotations in order to evaluate the adequate speed while keeping a reasonably good quality of the reconstruction (see below and Figure SM3).

The reference model is ideally reconstructed using unblurred 1D projections from a tilt series with an angular amplitude from -90° to +90° and an angular step of 0.1° in Figure 3b). Then it is compared with reconstructions performed without any blur in typical conditions used in conventional ET: an angular amplitude from -70° to +70° and angular steps of 1°, 2°, 3° and 5° respectively (Figure 3c). It should be noted that the missing wedge due to the limited tilting range produces a fading of the top and bottom edges of the silicalite-1 cage for all reconstructions (even un unblurred conditions). The images are then compared with the images reconstructed using projections having an integrated blur of 1°, 2°, 3° and 5° (Figure 3d). Considering the main microstructural features of the ghost, as the overall shape of the silicalite-1 and the presence of Ag nanoparticles, it can be seen that the rotation blur has a limited effect on the quality of the reconstructions up to at least 2°. At higher blur values, some of the smallest (2 to 4 nm) and the most decentered particles (such as the ones at the top of the image distant by 75 nm from the tilt axis) are lost, but this degradation is not significantly worse than that produced by a conventional tilting procedure with a step amplitude equivalent to the rotation blur.

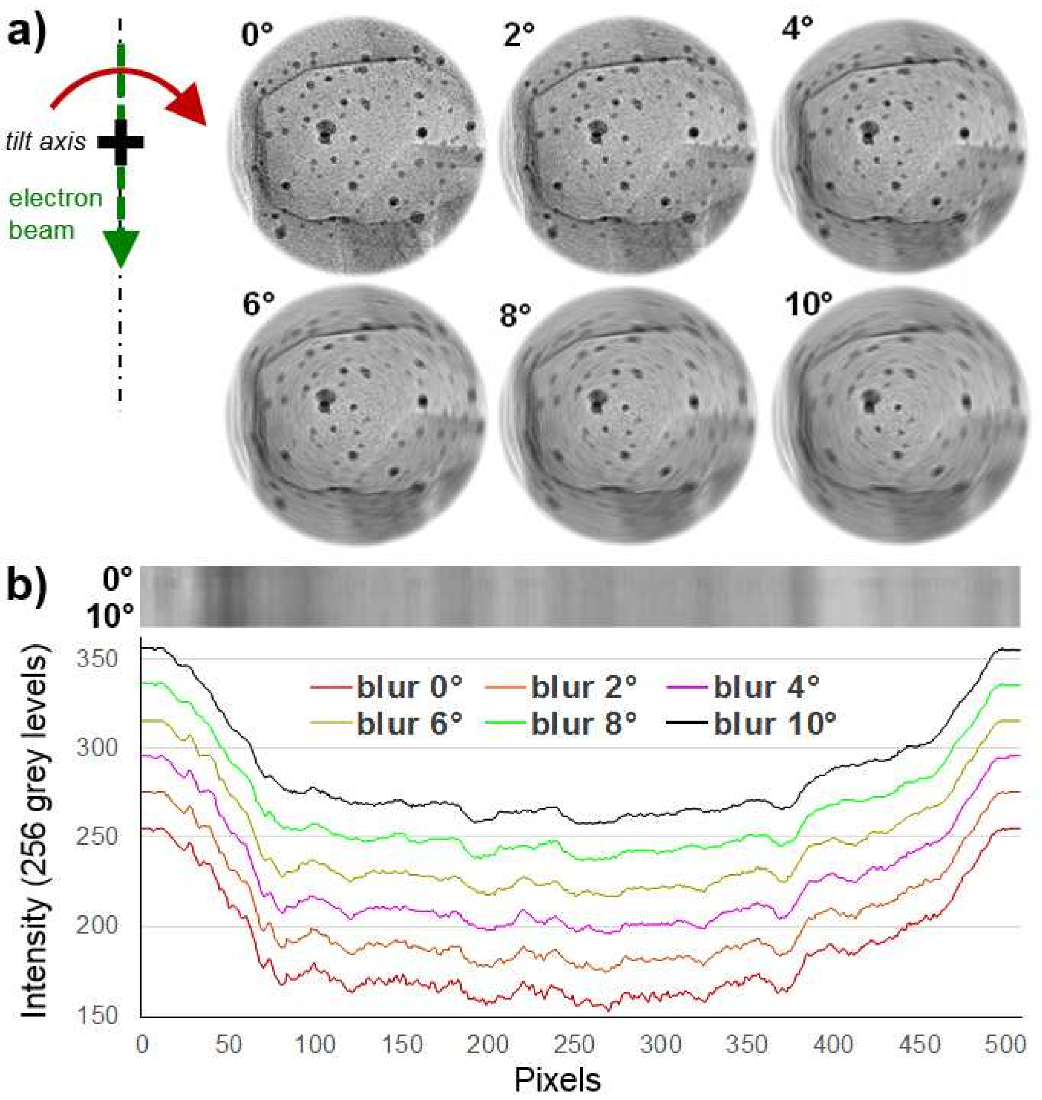

Figure 2: a) BF-TEM image showing Ag nanoparticles enclosed in silicalite-1 cages used as a phantom to simulate tomographic reconstructions using 1D projections recorded during a continuous rotation around a fixed rotation axis (black cross); the lateral size and the thickness (height) of the model correspond to a real microstructure of 150 nm. The blur was obtained after a rotation around the center of each phantom (small black marker. Note that using a tilt axis centered in the height of the object is not restrictive, the important parameter to qualify the blur amplitude is the distance of any details with respect to the center. Hence any conclusion drawn out from the present analysis will also apply to the case of an ex-centered tilt position corresponding to a possible bad eucentric alignment). The phantom at 0° is the reference having no blur integrated, then the model is shown with integrated rotation blurs of 2°, 4°, 6°, 8° and 10°. b) Enlarged 1D projections along the vertical beam axis of all phantoms with various blur levels; the graph shows the intensity profile of these projections. All data correspond to an untilted configuration. ***2-columns figure.***

The conclusion of such simulations is that we can continuously rotate the sample at speeds producing rotation blurs of up to 2° and still preserve the nanometric resolution in 3D. Accordingly, we can calculate the rotation blur α_{blur} produced in each frame during a CRRET experiment as a function of the total tilting range $2\alpha_{max}$ and the acquisition rate of the camera *fps*:

$$\alpha_{blur} = \frac{sample\ rotation\ speed}{camera\ frame\ rate} = \frac{2\alpha_{max}}{t_{total}\, fps} \qquad /1/$$

Where: - α_{blur} is the rotation blur in °/frame,

- $2\alpha_{max}$ is the angular interval in °,
- t_{total} is the total time of the rotation in s,
- *fps* is the camera recording rate expressed in number of frames per second.

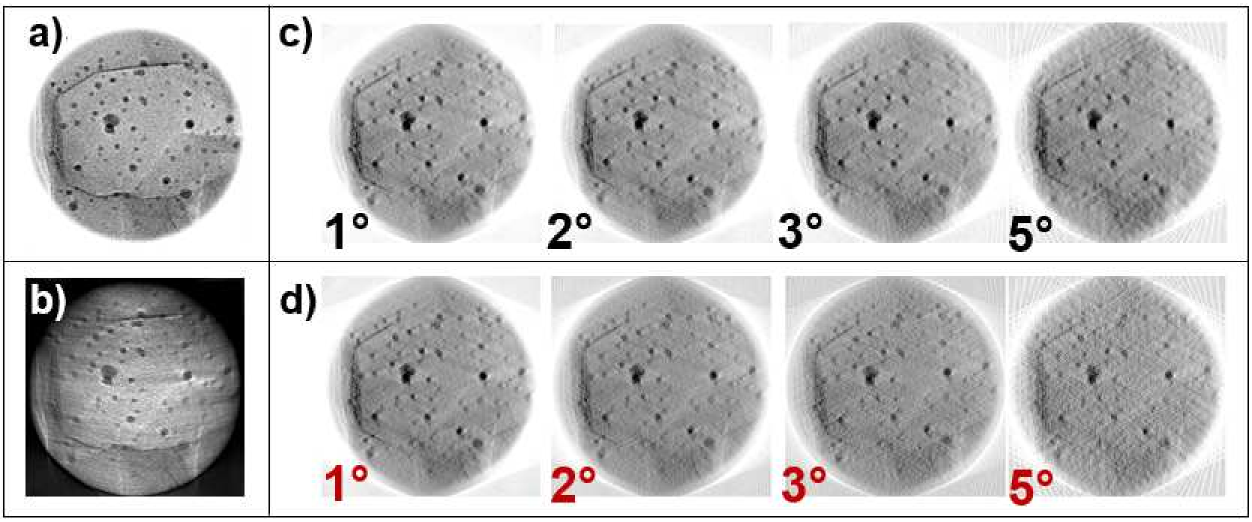

Figure 3: Reconstruction by the simple Weighted-Back Projection method of the 2D phantom introduced in Figures 2 and SM2 and recalled in a). b): reference reconstruction over the range +90° to -90° with an angular step of 0.1° (1801 1D projections). c): Conventional ET conditions, -70° to +70° with angular step of 1° (140 1D projections), 2° (70 1D projections), 3° (47 1D projections) and 5° (29 1D projections). d): Reconstructions from the 1D projections having an integrated blur of 1°, 2°, 3° and 5° as produced by CRRET with an increasing rotation speed. Note that most of the smallest particles at the top of the object (i.e. at 75 nm from the tilt position) are almost equally affected by the amplitude of the angular increment in conventional ET and the rotation blur in CRRET. ***2-columns figure.***

In Figure SM3 are plotted the recording speed of the camera in *fps* required to keep α_{blur} below the indicated values as a function of t_{total} for a given rotation amplitude $2\alpha_{max}$. This diagram shows that high-speed cameras capable of acquisition frequencies of hundreds of frames per second are easily compatible with experiments shorter than one second even with a rotation blur largely lower than the 2° limit evoked previously. The total acquisition time can even be shorter if the rotation amplitude is reduced from 140° to 120° or 100°. In practice, it seems that no TEM goniometer is yet capable to reach a rotation speed allowing to cover 140° in times shorter that about 3 s. Therefore, the limited factor for very fast CRRET is presently the microscope goniometer and not the acquisition speed of cameras.

All previous consideratios will be experimentally demonstrated for fast 'optimized' SBSET and CRRET respectively in the two successive sections 3 and 4.

3. Experimental results: fast SBSET acquisitions

3.1. Experimental setup

Experiments were performed using a FEI Titan ETEM (Cs-corrected) operating at 300 keV. A 2k UltraScan US1000XP-P Gatan CCD camera and a 4K Oneview Gatan CMOS camera were respectively used for the 'step-by-step' acquisitions reported in sections 3.2-3.3 and 3.4. The tilt series were aligned by IMOD [13], the volumes reconstructed by TomoJ [14] using the ART algorithm [8]. The data segmentation, visualization and quantification were performed by ImageJ [81] and 3D Slicer [82] softwares. Several samples have been used to demonstrate the possibilities of the different modes of fast ET.

3.2. SBSET) using a conventional CCD camera: Pd nanoparticles on δ-Al_2O_3 support

As previously mentioned in Table 1, the time consuming steps of the tilt series recording in classical SBSET are tracking and focusing of the object. We illustrate here successful fast SBSET experiments where the user performed the adjustments of the sample manually at each tilt position.

A first example concerns Pd/δ-Al_2O_3 catalysts used for the selective hydrogenation of alkynes and alkadienes into the respective olefins in petrochemical refining [83], see Figure 4. Details regarding the preparation of the TEM sample have been published previously [84].

The system is composed of Pd nanoparticles less than 5 nm in diameter supported on porous δ-Al_2O_3 consisting in aggregates of poorly crystalline platelets which produce only a weak diffraction contrast. Consequently, BF-ET is reasonably adapted as previously mentioned in section 1.1 and a classical automatic acquisition can then be compared to a fast 'semi-automatic' one. For the classical SBSET, the object was tilted from -74° to 66° using a step of 2° in Saxton mode [37]. The images were recorded in 2k x 2k pixels format with an exposure time of 1s (Figure 4a). The total acquisition time was 60 min using the FEI tomography software.

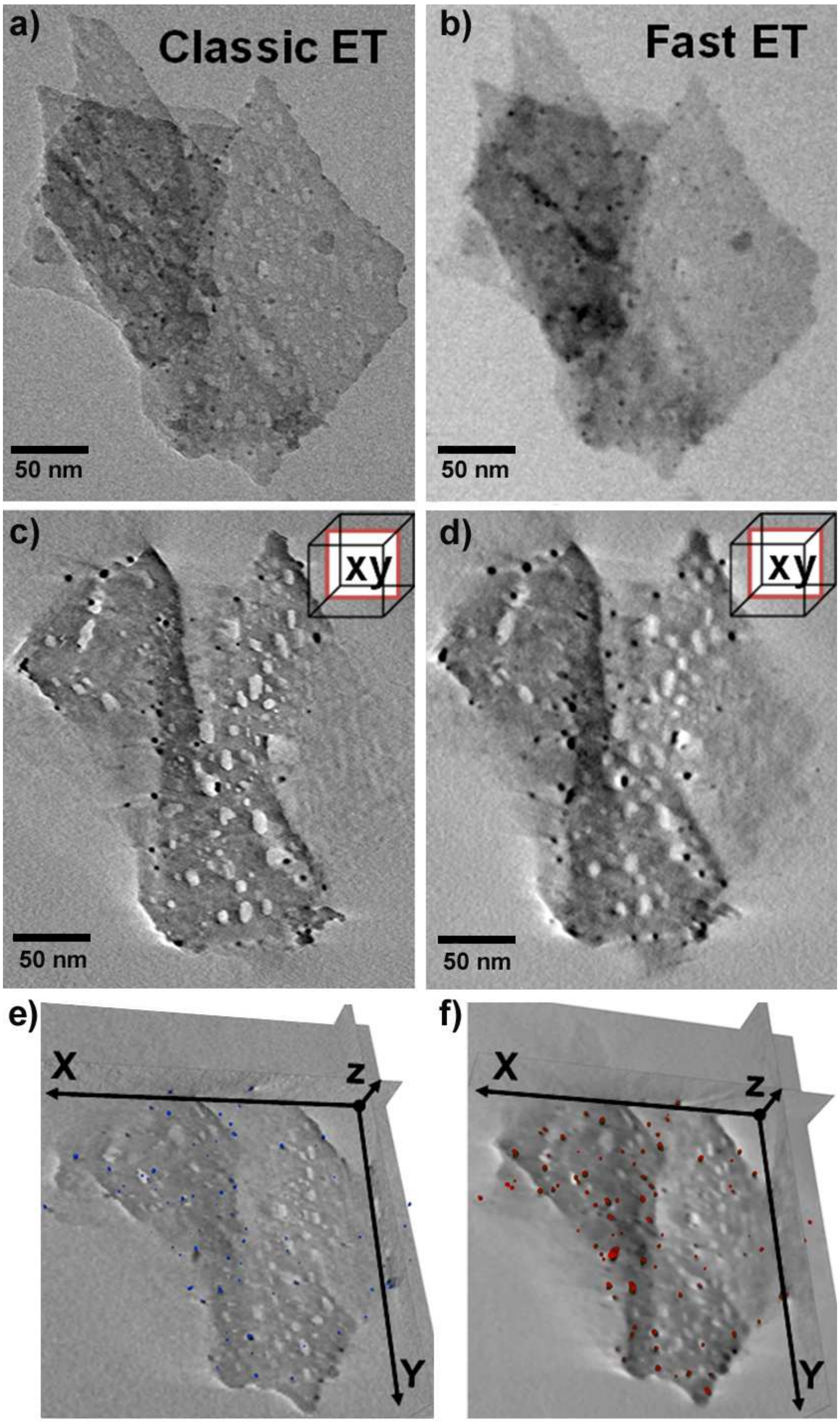

Figure 4: Comparison of classical 'step-by-step' with fast 'step-by-step' ET performed on a Pd/δ-Al_2O_3 sample (BF-TEM, 300 keV Titan ETEM). a) and b): BF projections at 0° from the classical and fast approaches respectively. c) and d): Cross sections of the reconstructed volumes at the same depth parallel to the (xy) plane; e) and f): Orthogonal cross sections showing the Pd particles distribution, in blue for classical SBSET and in red for fast SBSET. ***2-columns figure.***

For the 'semi-automatic' fast acquisition, the microscope was driven through a home-made plugin in DigitalMicrograph (GMS2 from Gatan) to tilt the holder with a step of 1° at maximum speed. After each step, a 1s alignment time was imposed in order to stabilize the goniometer and reduce undesirable blur. 1k x 1k pixels images were recorded with an exposure time of 0.1 s at each programmed tilt (Figure 4b). The total time needed to record the tilt series from -74° to 66° was 150 s (2 min 30 s) including the alignment and image acquisition times.

Figure 4c) and d) illustrate both reconstructions and report cross sections of a δ-Al_2O_3 platelet supporting Pd NPs. The section extracted from the volume calculated by classical SBSET (Figure 4c) exhibits a better contrast between the various components, i.e. Pd particles, pores and support than the section from the fast SBSET. This difference is due to the higher SNR in the projections having a longer exposer time, 1 s compared to 0.1 s. Nevertheless, the smallest pores and Pd particles are visible in the fast SBSET cross section (Figure 4d) despite lower SNR and numerical resolution. In Figure 4e-f) the Pd particles are highlighted in blue and red for the classcial and fast SBSET volumes respectively.

After segmentation, the Pd particle size distributions are quantified in 3D from both reconstructed volumes, converting their size into the diameter of the equivalent sphere for each particle (Figure 5). In the volume obtained by classical SBSET, 218 Pd particles were quantified, with an average diameter of 4.1 ± 0.8 nm whereas in the volume obtained by fast SBSET, 212 Pd particles were visible with an average size of 3.9 ± 0.7 nm. During the data segmentation of the fast tomography approach, only 6 Pd nanoparticles were lost, representing an error of 2.7% as compared to the SBSET 'reference' reconstruction. This experiment suggests that fast SBSET could give reliable results for the 3D analysis of nanomaterials while drastically decreasing the acquisition time and so the total electron dose supported by the sample. A more practical and detailed application of fast tomography during the in situ calcination of this Pd/δ-Al_2O_3 catalytic system performed in an ETEM has recently been published [84].

The next sections 3.3 and 3.4 illustrate that Fast SBSET can also be of a great interest for beam sensitive materials like biological samples and polymer-based materials respectively.

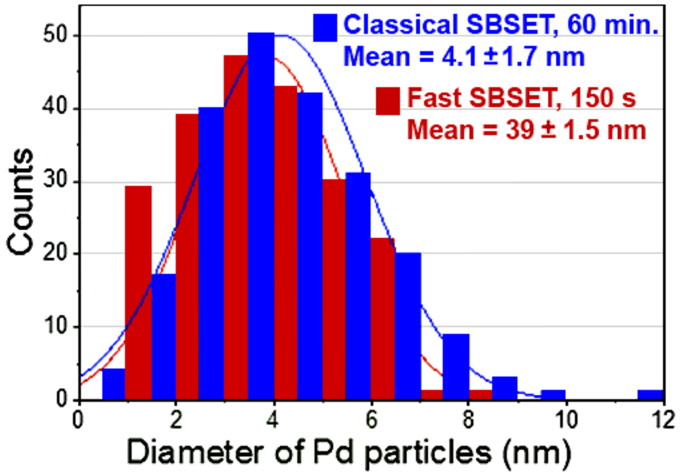

Figure 5: Distribution of Pd particle sizes obtained by classical SBSET in blue and by fast SBSET in red. The histograms represent the diameter of the spherical equivalent of each particle. The mean values are deduced from a Gaussian fit of both distributions. ***1-column figure.***

3.3. SBSET (step-by-step acquisitions) using a conventional CCD camera: magnetotactic bacteria

Pioneer work in electron tomography was indeed devoted to life sciences [21,22,23,85]. We chose the case of magnetotactic bacteria [86,87] because this system has already been studied by ET [26]. The bacteria were taken from a bacterial culture [88] grown in a liquid media by insulation. A portion was taken from the bacterial culture and transferred onto a holey carbon membrane supporting TEM grid after being chemically fixed. No other additional treatment or preparation step was performed on the sample.

The tilt range was limited to -50° to +50° because of shadowing from the supporting grid. Images were recorded every one degree with an exposure time of 0.1 s and an adjustment time of 0.5 s. 100 images were recorded at an image size of 1k x 1k pixels, each pixel representing 3.43 nm. The whole tilt series was acquired in 140 s. Figure 6a) shows the projection at 0°.

A cross section within the reconstructed volume parallel to the (xy) plane is shown in Figure 6b). Despite the limited tilt amplitude of 100°, a reasonable reconstruction was obtained. Figure 6c) shows a schematical model of the bacteria. Due to the thickness of the bacteria, of about 1 µm, details are not easily visible in the 2D projection. But in the cross section from the 3D reconstruction the cell membrane, the inclusion bodies, the flagella and the magnetosomes become clearly visible and comparable to the schematic representation.

In biology, the electron dose accepted in an image of an unstained vitrified biological sample in the TEM mode is typically between 1 and 12 $e^-/Å^2$ [89,90] whereas for a 3D analysis of a frozen biological sample [90], the maximal accepted electron dose should not exceed about100 $e^-/Å^2$. By using a high sensitivity camera, elementary frames recorded in 0.05 s/frame can be adjusted so that the sample receives a dose of about $1e^-/Å^2$ per frame. Thus, for 100 frames the total dose is of about 100 $e^-/Å^2$.This corresponds to a total acquisition in 5 s in the CRRET mode, a performance readily accessible for a tilt from -70 to +70°. It becomes then clearly possible to plan tomographic experiments on unstained biological materials in the continuous rotation mode.

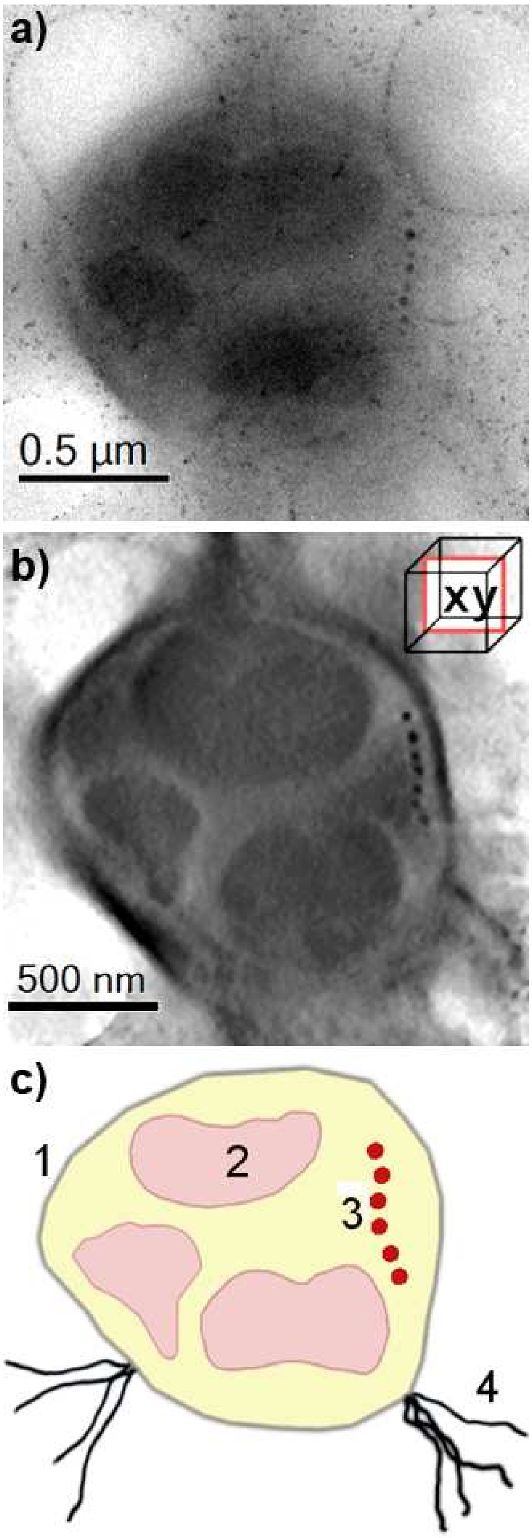

Figure 6: a) 0° 300 kV BF image of a chemically stained magnetotactic bacteria. b) Cross section parallel to the (xy) plane from the reconstructed volume obtained in 140 s by Fast SBSET. c) Schematical model showing (1) the cell wall, (2) phosphorus-rich ultrastructure bodies, (3) magnetosomes made of Fe and (4) flagella. Both images in a) and b) have been gamma-corrected to insure a better visibility of the Fe-particles (3). ***1-column figure.***

3.4. SBSET (step-by-step acquisition) using an optimized CMOS or DE-type camera: LDH-Latex polymer nanocomposite

Another typical example of beam sensitive materials for which fast ET would be profitable concerns polymers. We have investigated here a polymer nanocomposite made of a soft latex, methyl methacrylate (MMA), butyl acrylate (BA)-based matrix reinforced with Mg_3AlCO_3 layered double hydroxide nanoplatelets (LDH with a complete formula $[Mg^{2+}_{1-x}\ M^{3+}_{x}(OH)_2](CO3)^{2-}_{x/2}\ mH_2O$) [91], see Figure 7. The experiment was conducted on a slice prepared by cryo-ultramicrotomy at a thickness of about 100 nm (see more details in [91]); the sample was deposited on a usual Cu TEM grid mounted on a single tilt tomographic TEM holder from Fischione and imaged at 300 kV using the Oneview^{TM} camera from Gatan. Preliminary irradiation tests (see section SM-2 and video SM_2_polymer-irradiation-test.avi) allowed to define a critical dose of about 8.4 10^5 e^-/nm^2 in order to avoid significantly visible irradiation damage. According to this limit, reasonable parameters were adjusted to keep the electron dose received by the sample during the acquisition of a tomographic tilt series over a tilting amplitude of 140° below this value, i.e. around 8 10^5 e^-/nm^2: This was performed in the fast SBSET mode in only 200 seconds (see SM-2) under an electron flux of 4025 e^-/nm^2s. Although the electron flux differs in both acquisitions (irradiation test and true tomographic experiment), keeping the total dose below the critical value defined by the irradiation sequence gives more confidence in the representativeness of the reconstructed microstructure.

In Figure 7a) an image at 0° tilt of LDH platelets in the polymer matrix is shown; the black dots are the 5 nm Au nanoparticles used to align the tilt series and the grey lines are the reinforcing mineral platelets. Figure 7b) shows the 3D distributions of the LDH platelets within the volume of the nanocomposite. Figure 7c) is a cross-section through the volume (see video SM_2_polymer-tomogram.avi for the reconstructed tomogram). As in many other cases where LDH are incorporated into a polymer matrix (e.g. [92,93]) the mineral layers are mostly found in an exfoliated state. A spacing of elementary LDH layers at 0.8 nm is shown in the detail from Figure 7d). This interlayer distance is very close to the expected bilayer value of 0.75 – 0.8 nm [94], further refined as 0.759 – 0.793 nm [95] depending of the exact Mg/Al ratio. Note that this result comes from the volume reconstruction and not from a single experimental projection, giving at least the evidence that a voxel resolution better than 1 nm^3 has been achieved in this experiment, although the acquisition was performed in only 200 s. Such a result can be quantitatively used to establish relationships between the distribution of the reinforcing fillers and physical properties, such as mechanical properties, of the nanocomposites [96].

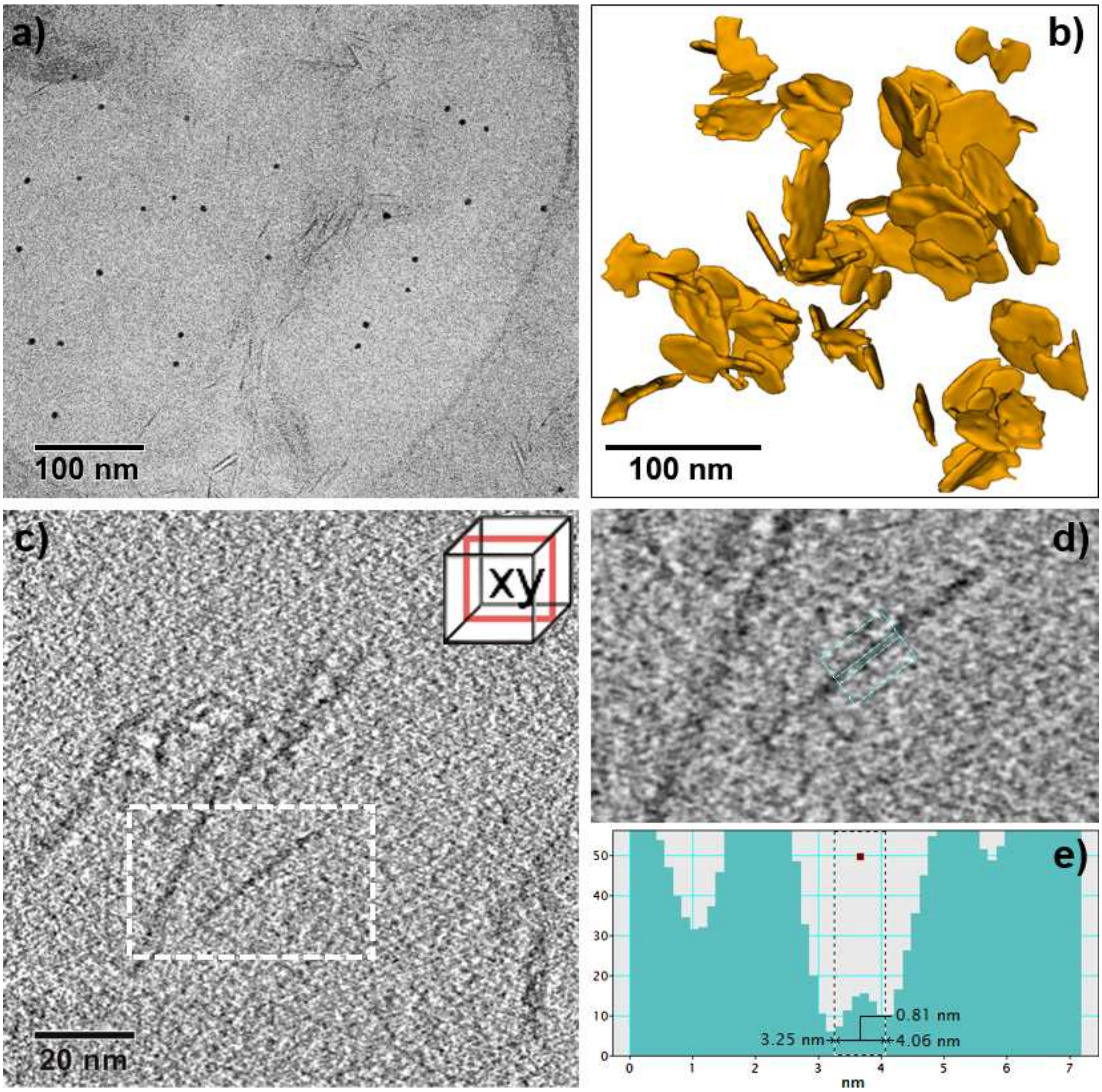

Figure 7: a) BF projection of the LDH-Latex nanocomposite at 0° (4k x 4k image, 300 kV); the black dots are the Au 5 nm fiducial markers, the grey lines are the LDH lamellas. b) 3D model from the fast SBSET reconstruction illustrated in c) representing the LDH nanoplatelets distribution within the latex matrix (not shown). c) Typical 1k x 1k elementary cross-section (single frame over 1050 frames) of the tomogram parallel to the (xy) plane; d) enlargement of the central region in c) (dotted rectangle) after averaging over 10 frames; e) intensity profile across the central platelet in d) showing a contrast compatible with the resolution of its bilayer structure near 0.8 nm. ***2-columns figure.***

4. Towards operando real time tomography: very fast CRRET acquisitions

4.1. Experimental setups

As for SBSET acquisitions, two experiments were performed using the FEI Titan ETEM (Cs-corrected) operating at 300 keV. For the first experiment the microscope was equipped with the UltraScan 2K US1000XP-P Gatan CCD. For the second one, a 4k Oneview Gatan camera was used. The first experiment aims at validating the consistency of the fast continuous rotation approach by comparing it to a classical tomography performed in the STEM-HAADF mode. A sample of Pd nanoparticles deposited on a α-Al$_3$O$_3$ support was prepared in conditions comparable to those described previously for the similar Pd/δ-Al_2O_3 system. Experimental details regarding the acquisition of the tilt series are given in section 4.2. Volume reconstructions were performed as described in section 3.

The second experiment aims at demonstrating the capabilities of fast CRRET under environmental conditions in an ETEM. The sample is a catalytic system made of shape-controlled Pd nanoparticles embedded into silica shells [97]. The temperature was raised up to 500°C with a dedicated MEMS-based Widlfire heating holder from DENSsolutions and using a specific S5 Si/SiN_x nanochip. This equipment provides tilting capabilities of ±72° without shadowing of the central thin windows, making it a well-adapted tool for ET at high temperature and under gas in the ETEM. Observations were done under reducing conditions (pure hydrogen pressure of 4 mbar), one of the preparation step of such catalysts [97].

According to the restrictions on the electron dose (see details in section 4.3), all recorded projections have a relatively low signal-to-noise ratio. The reconstruction was then performed with a home-made reconstruction algorithm named SIRT-FISTA-TV [64,98] using the MATLAB-GPU toolbox ASTRA [16] and which is very robust to noise. SIRT-FISTA-TV is based on the classical SIRT approach [9] and integrates Total Variation (TV) regularization [99] to deal with missing data. The Fast Iterative Shrinkage-Thresholding Algorithm (FISTA) [100] was used to speed up the convergence of the algorithm.

4.2. CRRET (Continuous Rotation and Recording Electron Tomography) using a conventional CCD-based camera: Pd nanoparticles on a α-Al_2O_3 support

Pd /α-Al_2O_3 constitutes a catalytic system very similar to Pd /δ-Al_2O_3; it is used in the petrochemical industry as heterogeneous catalyst for selective hydrogenation of acetylene in ethylene-rich streams (C2 hydrorefining) [101]. Contrarily to δ-Al_2O_3 grains, the α-Al_2O_3 phase is much less sensitive to the electron beam material but presents a stronger diffraction contrast: it is thus a good system to test the limits of fast tomography in the BF mode. An additional challenge is here to detect properly the very small Pd nanoparticles of about 3 nm in diameter dispersed on the alumina grains. Due to the diffraction contrast of the support and because a good Z-contrast is expected between Pd and α-Al_2O_3, a reference tomography experiment was performed in the STEM-HAADF mode. The HAADF tilt series was recorded from -75° to +61° with a 2° angular step using a conventional approach taking 90 minutes (Figure 8a). Prior to it, a continuous rotation acquisition of BF projections was performed over the same angular range (Figure 8b).

The CCD camera was used in the live mode displaying images at 10 fps, i.e. an acquisition time of 0.1 s per frame. To insure a negligible rotation blur, the rotation of the goniometer was performed with a low speed: 0.56°/s, leading to 240 s for covering the entire tilt range of 136°. According to relation /1/, these conditions led to a very negligible rotation blur of 0.05°/frame. This slow motion also allowed to manually track the object to keep it in the field of view. Video sequences were recorded by grabbing the 8 bits display of the camera using the free software Camstudio v.2.0 [102] at an acquisition rate of about 25 fps, thus duplicating all images displayed by the camera. After suppressing the repeated images, 2400 images were obtained (10 fps during 240 s). A lot of them were exhibiting a severe motion blur, especially when the stage was shifted manually to bring the object back in the center of the field of view. After removing the worst images based on their poor sharpness and SNR, only 76 frames were kept roughly uniformly distributed over the entire tilt range. It should be noted that this final number was chosen to be typically comparable to that of a conventional ET acquisition with a constant step of 2° over a tilt amplitude of the order of 140°. This means that skipping low quality frames from a continuous rotation experiment, even if they represent a large proportion of the acquisition, is not specifically restrictive.

Figure 8c) and d) compare STEM-HAADF and CRRET reconstructions. We have selected here on purpose a section showing the limitation of the BF tomography due to diffraction contrast. In the STEM-HAADF reconstruction, all Pd particles (brighter dots, highlighted by the green circles) anchored at the α-Al_2O_3 surface are clearly resolved. In the CRRET reconstruction, some of the smallest Pd particles (dark dots) are not detected because of a strong diffraction contrast at the edge of the alumina grain. The 3D models and the size histograms reported respectively in Figure 8e) and f) and Figure 9 confirm this poorer quality of the BF tomography. Only 60% of the smallest Pd nanoparticles were detected in the CRRET reconstruction although the average size measured from this fast tomography approach remains very close to the value measured from the STEM-HAADF conventional ET experiment. The poorer imaging performances are primarily imputable to the BF mode and secondarily to the fast approach. It should be noted that this experiment, although performed in the continuous recording mode, remains slower that an optimized SBSET acquisition as evaluated in Table 1: 1min 31 s, i.e. less than 100 s as compared to 240 s here. We will see in the next section that using a fast camera allows speeding up considerably the acquisition in the range of a few seconds.

4.3. Toward *Operando* CRRET using an optimized CMOS camera: sintering-resistant Pd@SiO_2 core-shell nanocatalysts under hydrogen up to 500°C

As indicated previously, one of the main interests of fast ET is to follow the morphological evolution of nanomaterials under dynamic conditions as it is the case of nanocatalysts exposed to gas and temperature in the ETEM. To demonstrate the capabilities of very fast tomography acquisitions under such environmental conditions, we chose a core-shell Pd@SiO_2 catalyst used for the methanation of

CO_2 (details of the synthesis and the catalytic properties have been reported previously [97]). Embedding the metallic nanoparticles into silica shells as seen in Figure 10a) aims at preventing significant sintering during the heat treatments used in the preparation of the catalysts, such as calcination and reduction up to possibly 400°C to 500°C. When the resistance to sintering can classically be quantified through 2D or even 3D TEM particle size measurements before and after these treatments [50], only an in situ analysis can provide direct and accurate information about the evolution as a function of time and temperature.

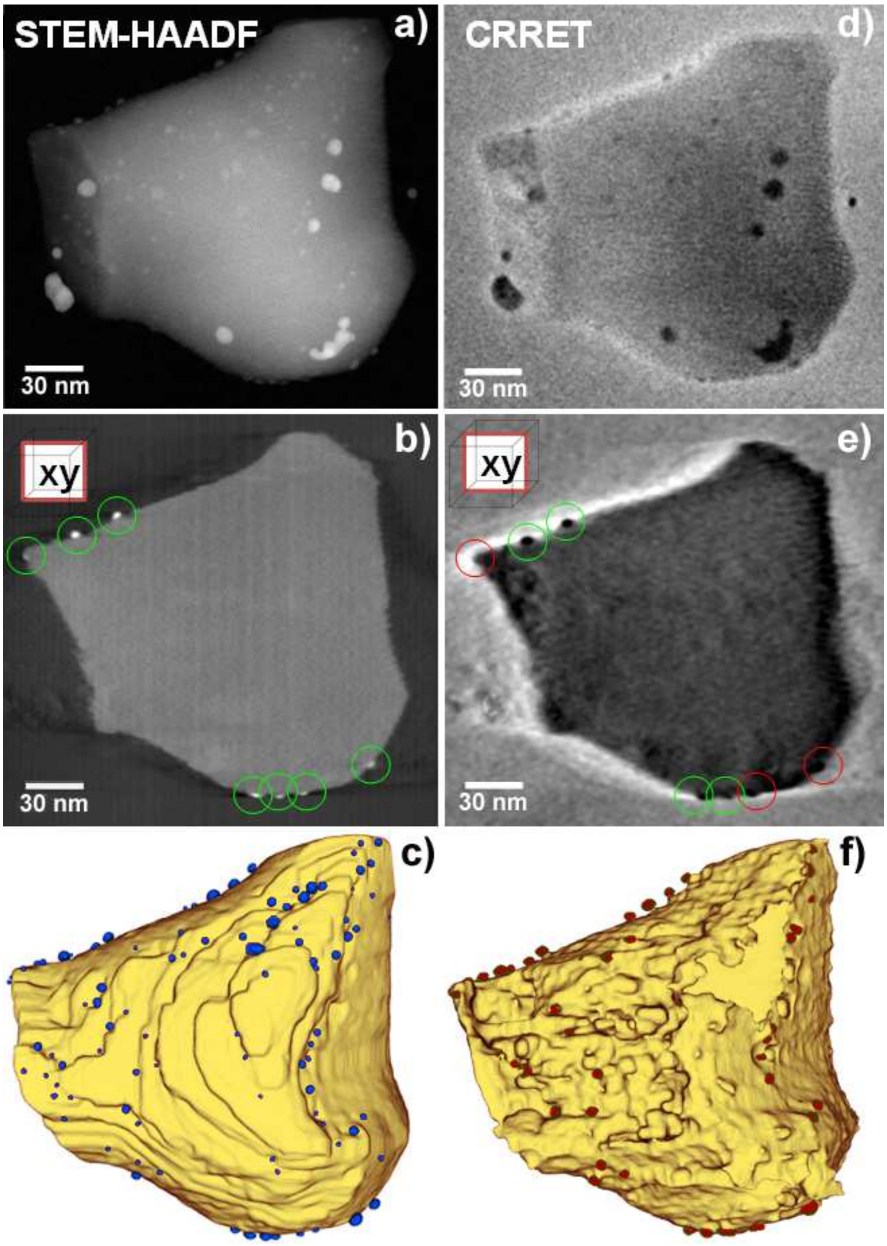

Figure 8: Comparison of conventional STEM-HAADF ET approach (a-c) with CRRET (d-f). a) 0° tilt HAADF image from a conventional tilt series recording on a α-Al_2O_3 grain supporting Pd nanoparticles. b) Near central cross-section parallel to the (xy) plane through the reconstructed volume. c) 3D model showing in blue Pd particles distributed over the α-Al_2O_3 support (in fade yellow). d-f): Images similar to a-c) for the CRRET experiment; the (xy) cross-section in e) is at the same depth than in b); Pd particles are shown as red dots in f). ***2-columns figure.***

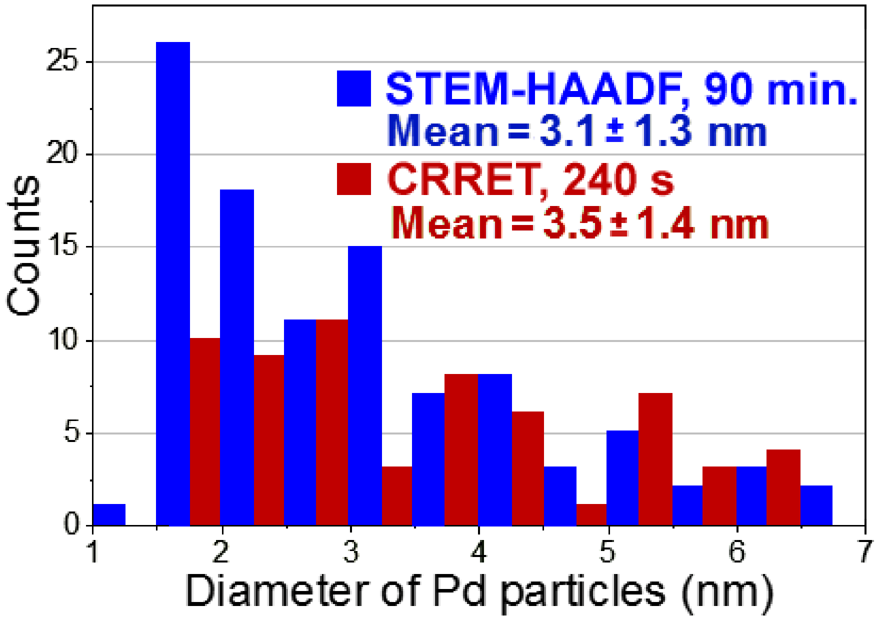

Figure 9: Pd particles size distributions, in blue analyzed by STEM-HAADF conventional electron tomography and in red by CRRET. Due to the diffraction contrast, some of the Pd particles are lost in the BF mode. ***1-column figure.***

Figure 10 shows the evolution of an isolated Pd@SiO_2 aggregate from 20°C under high vacuum to 400°C and 500°C during the in situ reduction under 4 mbar of pure hydrogen. Further details of this experiment, which comprises 7 tomographic series recorded in the CRRET mode in 43 seconds (6 to 9 s each acquisition) are given in section SM-3, which also includes the methodology used to control the radiation damage. Figure 11a to c) are single frames at a low tilt angle extracted from video sequences acquired at 20, 400 and 500°C respectively. The better contrast of the image at 20°C is due to the much lower pressure and temperature. The recorded video sequence of the tilt series for the last acquisition at 500°C in about 7 seconds is illustrated by the movie file SM_3_Pd-SiO2_500°C_4mbar-H2_CRRET.avi) displayed at real speed. Figure 10 d-f) show 3D models created from the tomograms reconstructed from the tilt series illustrated in Figure 10 a-c). Histograms of Pd NP size can then been measured from these 3D data as reported in Figure 10 g-i). Such measurements are more accurate and representative than what can be performed from simple 2D projections, since a close inspection of the 3D models (see video SM_3_Pd-SiO2_20-400-500°C_4mbar-H2_3D-models.avi showing an animation of these models) points out the existence of facets which may lead to errors in the evaluation of volumes from an extrapolation of 2D projections. Obviously the histograms have a low statistical meaning since they concern a very limited number of Pd nanoparticles, however they are deduced from the analysis of the same and unique object at different steps of its evolution.

The final conclusion of this experiment is that fast tomography has permitted to follow the reduction process in situ in the ETEM. Although a generalized growth and sintering of the core metallic particles can be ruled out, the present 3D analyses performed on the same Pd@SiO_2 aggregate shows a tendency of both size increasing (mean equivalent spherical diameter of about 16, 17 and 19 ± 0.5 nm at 20, 400 and 500°C respectively) and particles number decreasing (20 to 16 from 20 to 500°C) that evidences coalescence. This means a probable decrease of the specific surface of active phase of the heterogeneous catalyst.

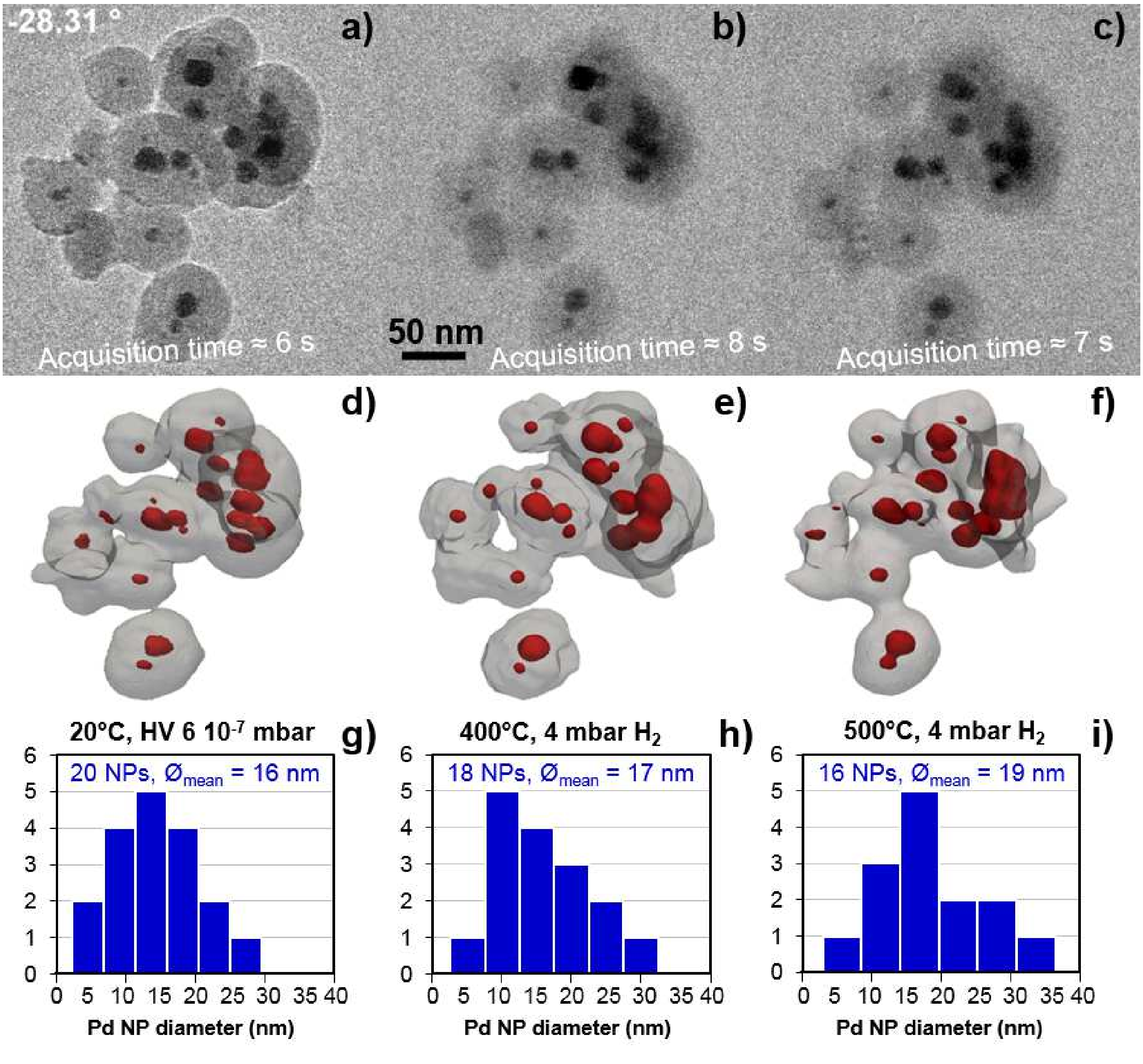

Figure 10: CRRET experiment of a Pd@SiO_2 aggregate reduced under 4 mbar of hydrogen in situ in ETEM. a-c): projections at a low tilt angle (about -28°) respectively at 20°C, high vacuum (6 10^{-7} mbar), 400°C (after 35 minutes under 4 mbar of H_2) and 500°C (after 60 minutes under 4 mbar H_2). Recording times for the entire tilt video sequence from +72° to -71° are as indicated. Pd nanoparticles (in dark) are embedded into silica beads. d-f): 3D models showing the reconstructed volumes corresponding to a-c) as seen under a similar viewing direction. g-i): Histograms of size distribution of Pd NPs considered as spheres.

5. Discussion and conclusions

The present work could constitute a possible starting point for a real time 3D investigation of nanomaterials exposed to temperature and gas conditions, yet restricted to the conventional bright field TEM mode because of too long acquisitions in the STEM mode.

With conventional digital CCD-based cameras, one can consider that reasonable acquisition times for a single image can be as short as 0.2 - 0.1 s. With the fast semi-automatic SBSET, where manual (x,y,z) adjustment of the projected images is done during a short time at each tilt (see Table 1), a total acquisition time slightly lower than 2 minutes can be achieved for an angular range of 140°. Although not suitable for the in situ 3D investigation of rapid dynamic processes, this semi-automatic Fast Step-by-Step Electron Tomography is nevertheless applicable to environmental investigations where the kinetics can be sufficiently slowed down by a fine control of the temperature and the gas pressure [51]. It further does not require any specific equipment or advanced software since the user can control any step of the acquisition manually or, better, semi-automatically with a simple script.

Real time tomography definitely requires simultaneous the high-speed rotation of the sample and acquisition of image. High-speed cameras available nowadays allow very fast acquisitions at several hundreds of frames per second. The analysis of the rotation blur, i.e. the blur due to the motion (rotation) of the sample during the recording of each projection shows that this effect is negligible even for very fast tilting of the goniometer (Figures 3, SM2 and SM3). Typically, a rotation speed of 140°/s would produce a rotation blur of 1.4°/frame while tilting from -70° to 70° with a camera frame rate of 100 fps. Under these conditions, the acquisition time of the tomographic series in the CRRET mode would be only one second. Consequently, the rotation speed of the microscope goniometer appears to be the limiting factor.

The feasibility of true ETEM operando tomography was previously demonstrated and already performed at a much moderate but still high speed [51]. To allow routine application of our faster approach, some improvements have to be made and the following obstacles have to be overcome:

(i) In a few seconds (typically 5 to 10), there is almost no time for a live adjustment of the focus (z change) and the possible in-plane drifts (x,y) of the goniometer, which can be of a few tens of nm [63]. It is also very difficult to account for non-systematic instabilities such as those possibly inherent to the goniometer when rotated at high speed. Then, keeping the object within the field of view while insuring a reasonable spatial and pixel resolutions with an adapted magnification remains a critical step. Technical progress allowing smoother rotations of the goniometer would then certainly be appreciable. Nevertheless, reproducible (x,y) drifts can be a priori calibrated, pre-recorded and a correction can be applied during the acquisition as it is already possible by using several existing softwares. It will however be of the outermost importance to perform the pre-calibration procedure as fast as possible to prevent the evolution of the sample submitted to environmental conditions. The goniometer pre-calibration can be done in an area close to the region of interest as classically performed in low-dose experiments to protect it from the electron beam influence. Ongoing works will address such developments to correct the (x,y) drifts. Maintaining the focus during the tilt sequence is much less trivial. Methods exist to perform this adjustment: they generally consist in tilting the beam in two opposite directions and deducing (and further correcting) the defocused value from the displacement between the two images [31,36,103]. This procedure is however time consuming and not easy to implement during a fast frame rate recording; it may be incompatible with experiments at the level of a few seconds.

(ii) Despite the relatively short acquisition time, the Continuous Rotation and Recording Electron Tomography (CRRET) experiments will produce a very large amount of data due to the very high recording rate and large images size (16 MB for a real 2k image). Following the kinetics of any reaction requires recording several tilt series of the same or similar object(s). This may then easily lead to TBytes of data in a very short time and to severe challenges in terms of handling, transfer, storage and processing.

Beyond operando tomography, CRRET also presents advantages for the study of electron beam sensitive materials (e.g., biological and polymer-based samples such as shown in Figures 6 and 7). The counterpart of fast acquisition is the degradation of the signal-to-noise ratio, which can become a limiting factor in some specific cases. A positive point is however that in all reported experiments, the final resolution remains very comparable to usual ET: particles as small as 1-2 nm have been quantified in the case of Pd on δ and α-Al_2O_3 y. In addition, a sub-nm resolution has been reached in the case of the polymer-nanocomposite shown in Figure 7.

In conclusion, the Continuous Rotation and Recording Electron Tomography approach presents a considerable interest for the study of phase transformations or reactions of nanomaterials that can be followed in an Environmental TEM. This is a first step towards 3D analysis of in situ straining experiments [75] which remains another exciting topic.

Acknowledgements

We would like to thank CLYM (www.clym.fr) for the access to the FEI 80-300 keV ETEM microscope. Acknowledgements are due to Dr. Priscilla Avenier for her help in the sample synthesis. We are grateful to Dr. Cécile Cottin-Bizonne and Dr. Yannick Tauran for providing the bacteria sample, and to Chenxi Ma and Khyatee Sethi for their contribution to some tomographic reconstructions. Gatan and DENSsolutions are acknowledged for their interest in the development of fast environmental electron tomography.

Funding

This work was financially supported by IFP Energies Nouvelles, the INSA BQR program (project Spee3D 2015-0020), the 3Dclean ANR-15-CE09-0009 project granted by The French National Research Agency and the network METSA (FR3507 CNRS). It was also supported by the LABEX iMUST (ANR-10-LABX-0064) of Université de Lyon, within the program "Investissements d'Avenir" (ANR-11-IDEX-0007) operated by the French National Research Agency (ANR). S.K. thanks the French Ministry of Higher Education and Research for his PhD grant.

Authors contributions

S.K., L.R. and T.E. performed all TEM experiments reported in this work. F.D. contributed to the observations of the polymer-based system described in Figure 7. A.S.G. and A.C. have participated to the preparation of catalytic samples (Pd-Al_2O_3 and Pd-SiO_2). C.L. has contributed in developing a script to facilitate the acquisition of optimized step-by-step tilt series. T.G., H.B. and V.M. worked on the development of a regularized reconstruction algorithm robust to noise. All co-authors discussed the results and contributed to write, improve the manuscript and have approved the present final version. T.E. directed the project as a coordinator of the ongoing French ANR project 3Dclean.

The authors declare no competing financial.

Data availability

The raw/processed data required to reproduce these findings cannot be shared at this time as the data also forms part of an ongoing study.

References

[1] D. B. Williams, C. B. Carter, Transmission electron microscopy: a textbook for materials science, Springer, New York, 2nd ed., 2008, 775 p.

[2] P. A. Midgley, R. E. Dunin-Borkowski, electron tomography and holography in materials science. Nat. Mater., 8 (2009), 271-280. https://doi.org/10.1038/nmat2406.

[3] T. Epicier, Tomographie électronique, chap. 3 in Imagerie 3D en mécanique des matériaux, Lavoisier S.A.S., Paris, 2014, pp. 83-–122.

[4] S. Carenco, S. Moldovan, L. Roiban, I. Florea, D. Portehault, K. Vallé, P. Belleville, C. Boissière, L. Rozes, N. Mézailles, M. Drillon, C. Sanchez, O. Ersen, The Core Contribution of Transmission Electron Microscopy to Functional Nanomaterials Engineering. Nanoscale, 8 (2016), 1260-1279. https://doi.org/10.1039/C5NR05460E.

[5] Z. Saghi, P.A. Midgley, Electron Tomography in the (S)TEM: From Nanoscale Morphological Analysis to 3D Atomic Imaging. Annu. Rev. Mater. Res., 42 (2012), 59-79. https://doi.org/10.1146/annurev-matsci-070511-155019.

[6] M.C. Scott, C-C. Chen, M. Mecklenburg, C. Zhu, R. Xu, P. Ercius, U. Dahmen, B.C. Regan, J. Miao, Electron tomography at 2.4-Angströms resolution. Nature, 483 (2012), 444-447. https://doi.org/10.1038/nature10934.

[7] S. Bals, B. Goris, A. De Backer, S. Van Aert, G. Van Tendeloo, Atomic resolution electron tomography. MRS Bulletin, 41 07 (2016), 525-530. https://doi.org/10.1557/mrs.2016.138.

[8] R. Gordon, R. Bender, G. T. Herman, Algebraic Reconstruction Techniques (ART) for Three-dimensional Electron Microscopy and X-ray Photography. J. Theor. Biol., 29 (1970), 471-481. https://doi.org/10.1016/0022-5193(70)90109-8.

[9] P. Gilbert, Iterative methods for the three-dimensional reconstruction of an object from projections. J. Theor. Biol., 36 (1972), 105-117. https://doi.org/10.1016/0022-5193(72)90180-4.

[10] B. Goris, T. Roelandts, K. J. Batenburg, H. Heidari Mezerji, S. Bals, Advanced reconstruction algorithms for electron tomography: from comparison to combination. Ultramicroscopy, 127 (2013), 40-47. http://dx.doi.org/10.1016/j.ultramic.2012.07.003.

[11] X. Zhuge, H. Jinnai, R. E. Dunin-Borkowski, V. Migunov, S. Bals, P. Cool, A.-J. Bons, K. J. Batenburg, Automated discrete electron tomography - Towards routine high-fidelity reconstruction of nanomaterials. Ultramicroscopy, 175 (2017), 87-96. https://doi.org/10.1016/j.ultramic.2017.01.009.

[12] R. Hegerl, The EM Program Package: A Platform for Image Processing in Biological Electron Microscopy. J. Struct. Biol., 116 (1996), 30-34. https://doi.org/10.1006/jsbi.1996.0006.

[13] J.R. Kremer, D.N. Mastronarde, J.R. McIntosh, Computer Visualization of Three-Dimensional Image Data Using IMOD. J. Structural Biology, 116 (1996), 71-76. https://doi.org/10.1006/jsbi.1996.0013.

[14] C. Messaoudi, T. Boudier, C. Sorzano, S. Marco, TomoJ: tomography software for three-dimensional reconstruction in transmission electron microscopy. BMC Bioinformatics, 8 (2007), 288. https://doi.org/10.1186/1471-2105-8-288.

[15] J.-I. Agulleiro, J.-J. Fernandez, Tomo3D 2.0 – Exploitation of Advanced Vector eXtensions (AVX) for 3D Reconstruction. J. Struct. Biol., 189 (2015), 147-152. https://doi.org/10.1016/j.jsb.2014.11.009.

[16] W. van Aarle, W. J. Palenstijn, J. De Beenhouwer, T. Altantzis, S. Bals, K. J. Batenburg, J. Sijbers, The ASTRA Toolbox: A platform for advanced algorithm development in electron tomography. Ultramicroscopy, 157 (2015), 35-47. https://doi.org/10.1016/j.ultramic.2015.05.002.

[17] S. Nickell, F. Förster, A. Linaroudis, W. Del Net, F. Beck, R. Heger, W. Baumeister, J.M. Plitzko, TOM software toolbox: acquisition and analysis for electron tomography. J. Structural Biology, 149 (2005), 227-234. https://doi.org/10.1016/j.jsb.2004.10.006. See also TOM Toolbox, URL: https://www.biochem.mpg.de/tom_ (accessed July 4, 2017).

[18] B.D.A. Levin, Y. Jiang, E. Padgett, S. Waldon, C. Quammen, C. Harris, U. Ayachit, M.s Hanwell, P. Ercius, D.A. Muller, R. Hovden, Tutorial on the Visualization of Volumetric Data Using tomviz. Microscopy Today, 26 1 (2018), 12-27. https://doi.org/10.1017/S1551929517001213. See also Tomviz, https://tomviz.org/ (accessed October 18, 2018).

[19] 3D Tomography Acquisition Software | Gatan, Inc., http://www.gatan.com/products/tem-imaging-spectroscopy/3d-tomography-acquisition-software (accessed February 17, 2017).

[20] P.W. Hawkes, The Electron Microscope as a Structure Projector, in Electron Tomography, ed. J. Frank, Springer, New York, NY, (2007), pp. 83–111.

[21] W. Baumeister, R. Grimm, J. Walz, Electron tomography of molecules and cells, Trends Cell Biol., 9 (1999), 81-85. https://doi.org/10.1016/S0962-8924(98)01423-8.

[22] J. Frank, Electron Tomography - Methods for Three-DimensionalVisualization of Structures in the Cell|, Springer-Verlag New York, 2006.

[23] M. Bárcena, A.J. Koster, Electron tomography in life science. Seminars in Cell & Developmental Biology, 20 (2009) 920–930. https://doi.org/10.1016/j.semcdb.2009.07.008.

[24] J. Hutchings, G. Zanetti, Fine details in complex environments: the power of cryo-electron tomography. Biochemical Society Transactions (2018). https://doi.org/10.1042/BST20170351.

[25] J. Zečević, K.P. de Jong, P.E. de Jongh, Progress in electron tomography to assess the 3D nanostructure of catalysts, Curr. Opin. Solid State Mater. Sci., 17 (2013), 115-125. https://doi.org/10.1016/j.cossms.2013.04.002.

[26] P. A. Midgley, M. Weyland, 3D electron microscopy in the physical sciences: the development of Z-contrast and EFTEM tomography. Ultramicroscopy, 96 (2003), 413-431. https://doi.org/10.1016/S0304-3991(03)00105-0.

[27] C. Kübel, A. Voigt, R. Schoenmakers, M. Otten, D. Su, T-C. Lee, A. Carlsson, J. Bradley,Recent Advances in Electron Tomography: TEM and HAADF-STEM Tomography for Materials Science and Semiconductor Applications. Microsc. Microanal., 11 (2005), 378–400. https://doi.org/10.1017/S1431927605050361.

[28] O. Nicoletti, F. de la Peña, R. K. Leary, D. J. Holland, C. Ducati, P. A. Midgley, Three-dimensional imaging of localized surface plasmon resonances of metal nanoparticles. Nature, 502 (2013), 80–84. https://doi.org/10.1038/nature12469.

[29] G. Möbus, R. C. Doole, B. J. Inkson, Spectroscopic electron tomography. Ultramicroscopy, 96 3-4 (2003), 433-451. https://doi.org/10.1016/S0304-3991(03)00106-2.

[30] K. Lepinay, F. Lorut, R. Pantel, T. Epicier, Chemical 3D tomography of 28 nm high K metal gate transistor: STEM XEDS experimental method and results. Micron, 47 (2013), 43-49. https://doi.org/10.1016/j.micron.2013.01.004.

[31] D. N. Mastronarde, Automated electron microscope tomography using robust prediction of specimen movements. J. Structural Biology, 152 (2005), 36-51. https://doi.org/10.1016/j.jsb.2005.07.007. See also SerialEM, http://bio3d.colorado.edu/SerialEM/ (accessed October 18, 2018).

[32] FEI Xplore3D™ The total solution for electron tomography on Titan™ and Tecnai. Application n ote DS0017 01-2008. http://www.cnf.umcs.lublin.pl/pdfy/Xplore_3D_web_ds.pdf (accessed October 18, 2018).

[33] Tomography 4.0 software, https://www.fei.com/software/tomography-4/ (accessed October 18, 2018).

[34] EM-05500TGP TEM Tomograph System | Products | JEOL Ltd., https://www.jeol.co.jp/en/products/detail/EM-05500TGP.html (accessed July 8, 2017).

[35] ResAlta Research Technologies - iTEM - the premier software platform for TEM, http://resaltatech.com/item_platform_main.htm (accessed October 18, 2018).

[36] C. Suloway, J. Shi, A. Cheng, J. Pulokas, B. Carragher, C. S. Potter, S. Q. Zheng, D. A. Agard, G. J. Jensen, Fully automated, sequential tilt-series acquisition with Leginon. J. Structural Biology, 167 (2009), 11-18. https://doi.org/10.1016/j.jsb.2009.03.019.

[37] W. O. Saxton, W. Baumeister, M. Hahn, Three-dimensional reconstruction of imperfect two-dimensonal crystals. Ultramicroscopy, 13 (1984), 57-70. https://doi.org/10.1016/0304-3991(84)90057-3.

[38] W. J. H. Hagen, W. Wan, J. A. G. Briggs, Implementation of a cryo-electron tomography tilt-scheme optimized for high resolution subtomogram averaging. J. Structural Biology, 197 (2017), 191-198. http://dx.doi.org/10.1016/j.jsb.2016.06.007.

[39] D.B. Carlson, J.E. Evans, Low-Dose Imaging Techniques for Transmission Electron Microscopy. chap. 5 in 'The Transmission Electron Microscope', (2012), ed. K. Maaz, www.intechopen.com. https://doi.org/10.5772/36614.

[40] E.P. Butler, K.F. Hale, In situ studies of gas-sold reactions, in: E.P. Butler, K.F. Hale (Eds.), Dynamic Experiments in the Electron Microscope, North Holland Pub. Company, Amsterdam, 1981, pp. 239-308.

[41] P.L. Gai, In-situ Microscopy in Materials Research, Springer Science+Business Media New York, 1997, 336 p.

[42] T.W. Hansen, J.B. Wagner, Controlled Atmosphere Transmission Electron Microscopy, Springer International Publishing Switzerland, 2016, 329 p.

[43] E.D. Boyes,P.L. Gai, Visualising reacting single atoms under controlled conditions: Advances in atomic resolution in situ Environmental (Scanning) Transmission Electron Microscopy (E(S)TEM), C.R. Physique 15 (2014), 200-213. https://dx.doi.org/10.1016/j.crhy.2014.01.002.

[44] J. Jinschek, Advances in the environmental transmission electron microscope (ETEM) for nanoscale. Chem. Commun., 50 (2014), 2696-2706. https://dx.doi.org/10.1039/c3cc49092k.

[45] S. Takeda, Y. Kuwauchi, H. Yoshida, Environmental transmission electron microscopy for catalyst materials using a spherical aberration corrector. Ultramicroscopy, 151 (2015), 178-190. https://dx.doi.org/10.1016/j.ultramic.2014.11.017.

[46] F. Tao, P.A. Crozier, Atomic-Scale Observations of Catalyst Structures under Reaction Conditions and during Catalysis. Chem. Rev., 116 (2016), 3487-3539. https://dx.doi.org/10.1021/cr5002657.

[47] Y. Yu, H. L. Xin, R. Hovden, D. Wang, E. D. Rus, J. A. Mundy, D. A. Muller, H. D. Abruña, Three-Dimensional Tracking and Visualization of Hundreds of Pt–Co Fuel Cell Nanocatalysts During Electrochemical Aging. Nano Lett., 12 (2012), 4417-4423. https://dx.doi.org/10.1021/nl203920s.

[48] G. Melinte, I. Florea, S. Moldovan, I. Janowska, W. Baaziz, R. Arenal, A. Wisnet, C. Scheu, S. Begin-Colin, D. Begin, C. Pham-Huu, O. Ersen, A 3D insight on the catalytic nanostructuration of few-layer graphene. Nat. Commun., 5 (2014), 4109. https://dx.doi.org/10.1038/ncomms5109.

[49] L. Han, Q. Meng, D. Wang, Y. Zhu, J. Wang, X. Du, E. A. Stach, H. L. Xin, Interrogation of bimetallic particle oxidation in three dimensions at the nanoscale. Nat. Comm., 7 (2016), 13335. https://dx.doi.org/10.1038/ncomms13335.

[50] W. Baaziz, M. Bahri, A-S. Gay, A. Chaumonnot, D. Uzio, S. Valette, C. Hirlimann, O. Ersen, Thermal behavior of Pd@SiO_2 nanostructures in various gas environments: a combined 3D and in-situ TEM approach. Nanoscale, 10 (2018), 20178-20188 https://doi.org/10.1039/C8NR06951D.

[51] L. Roiban, S. Li, M. Aouine, A. Tuel, D. Farrusseng, T. Epicier, Fast ‘Operando’ electron nanotomography. J. Microsc., 269 2 (2018), 117-126. https://dx.doi.org/10.1111/jmi.12557.

[52] M. Bieberle, U. Hampel, F. Barthel, H.-J. Menz, H.-G. Mayer, Ultrafast three-dimensional X-ray computed tomography. Applied Physics Letters, 98 (2011), 034101. https://doi.org/10.1063/1.3534806.

[53] W. Stanfod, J. A. Rumberger, Eds., Ultrafast Computed Tomography in Cardiac Imaging: Principles and Practice, Futura Publishing Company, Inc., Mount Kisco, NY, 1992, 351 p.

[54] R. Mokso, D. A. Schwyn, S. M. Walker, M. Doube, M. Wicklein, T. Müller, M. Stampanoni, G. K. Taylor, H. G. Krapp, Four-dimensional in vivo X-ray microscopy with projection-guided gating. Sci. Rep., 2015, 5, 8727. https://doi.org/10.1038/srep08727.

[55] F. Garcıa-Moreno, P.H. Kamm, T.R. Neu, J. Banhart, Time-resolved in situ tomography for the analysis of evolving metal-foam granulates, J. Synchrotron Rad. (2018) 25. https://doi.org/10.1107/S1600577518008949.

[56] J. R. Jinschek, K. J. Batenburg, H. A. Calderon, R. Kilaas, V. Radmilovic, C. Kisielowski, 3-D reconstruction of the atomic positions in a simulated gold nanocrystal based on discrete tomography: Prospects of atomic resolution electron tomography. Ultramicroscopy. 108 (2008), 589-604. https://doi.org/10.1016/j.ultramic.2007.10.002.

[57] S. Van Aert, K. J. Batenburg, M. D. Rossell, R. Erni, G. Van Tendeloo, Three-dimensional atomic imaging of crystalline nanoparticles. Nature, 470 (2011), 374–377. https://doi.org/10.1038/nature09741.

[58] Y. Yang, C.-C. Chen, M.C. Scott, C. Ophus, R. Xu, A. Pryor Jr., L. Wu, F. Sun, W. Theis,J. Zhou, M. Eisenbach, P.R.C. Kent, R.F. Sabirianov, H. Zeng, P. Ercius, J. Miao, Deciphering chemical order/disorder and material properties at the single-atom level. Nature, 542 7639 (2017), 75–79. https://doi.org/10.1038/nature21042.

[59] J. Park, H. Elmlund, P. Ercius, J. M. Yuk, D. T. Limmer, Q. Chen, K. Kim, S. H. Han, D. A. Weitz, A. Zettl, T. P. Alivisatos, Nanoparticle imaging. 3D structure of individual nanocrystals in solution by electron microscopy. Science, 349 (2015), 290-295. https://doi.org/10.1126/science.aab1343.

[60] M. Gemmi, M. G. I. La Placa, A. S. Galanis, E. F. Rauch, S. Nicolopoulos, Fast electron diffraction tomography. J. Appl. Cryst. 48 (2015), 718-727. https://doi.org/10.1107/S1600576715004604.

[61] L. Palatinus, P. Brázda, P. Boullay, O. Perez, M. Klementová, S. Petit, V. Eigner, M. Zaarour, S. Mintova, Hydrogen positions in single nanocrystals revealed by electron diffraction. Science, 355, 6321 (2017), 166-169. https://doi.org/10.1126/science.aak9652.

[62] B. L. Nannenga, D. Shi, A. G. W. Leslie, T. Gonen, High-resolution structure determination by continuous-rotation data collection in MicroEDED Nat. Methods, 11 (2014), 927-930. https://doi.org/10.1038/nmeth.3043.

[63] V. Migunov, H. Ryll, X. Zhuge, M. Simson, L. Strüder, K. J. Batenburg, L. Houben, R. E. Dunin-Borkowski, Rapid low dose electron tomography using a direct electron detection camera. Sci. Rep., 5 (2015), 14516. https://doi.org/10.1038/srep14516.

[64] H. Banjak, T. Grenier, T. Epicier, S. Koneti, L. Roiban, A.-S. Gay, I. Magnin, F. Peyrin, V. Maxim, Evaluation of noise and blur effects with SIRT-FISTA-TV reconstruction algorithm: Application to fast environmental transmission electron tomography. Ultramicroscopy, 189 (2018), 109-123. https://doi.org/10.1016/j.ultramic.2018.03.022.

[65] G. McMullan, A. R. Faruqi, D. Clare, R. Henderson, Comparison of optimal performance at 300keV of three direct electron detectors for use in low dose electron microscopy.Ultramicroscopy, 147 (2014), 156-163. https://doi:10.1016/j.ultramic.2014.08.002.

[66] Falcon 3EC Direct Electron Detector, https://www.fei.com/accessories/falcon-3ec-direct-electron-detector/ (accessed October 21, 2018).

[67] M. Kuijper, G. van Hoften, B. Janssen, R. Geurink, S. De Carlo, M. Vos, G. van Duinen, B. van Haeringen, M. Storms, FEI's direct electron detector developments: Embarking on a revolution in cryo-TEM. J. Structural Biology, 192 (2015), 179-187. https://doi.org/10.1016/j.jsb.2015.09.014.

[68] K2 IS camera | Gatan, Inc., http://www.gatan.com/products/tem-imaging-spectroscopy/k2-camera (accessed October 21, 2018).

[69] K3 camera, | Gatan, Inc., http://www.gatan.com/k3-camera (accessed October 17, 2018).

[70] Direct Electron, LP - DE-Series Cameras, http://www.directelectron.com/products/de-series (accessed October 17, 2018).

[71] PNSensor | Detector Concept of pn-CCDs, http://www.pnsensor.de/Welcome/Detectors/pn-CCD/index.php (accessed October 17, 2018).

[72] Ceta 16M, https://www.fei.com/accessories/ceta-16m/ (accessed October 17, 2018).

[73] OneView 16-Megapixel Camera for TEM Applications | Gatan, Inc., http://www.gatan.com/products/tem-imaging-spectroscopy/oneview-camera (accessed July 10, 2017).

[74] TemCam XF-Series, http://www.tvips.com/camera-systems/temcam-xf-series/ (accessed October 17, 2018).

[75] S. Hata, S. Miyazaki, T. Gondo, K. Kawamoto, N. Horii, K. Sato, H. Furukawa, H. Kudo, H. Miyazaki, M. Murayama, In-situ straining and time-resolved electron tomography data acquisition in a transmission electron microscope. Microscopy (2016), 1-11. https://doi:10.1093/jmicro/dfw109.

[76] K. Sato, H. Miyazaki, T. Gondo, S. Miyazaki, M. Murayama, S. Hata, Development of a novel straining holder for transmission electron microscopy compatible with single tilt-axis electron tomography. Microscopy, 64 (2015), 369–-375. https://doi:10.1093/jmicro/.

[77] Z. Saghi, D. J. Holland, R. Leary, A. Falqui, G. Bertoni, A. J. Sederman, L. F. Gladden, P. A. Midgley, Three-Dimensional Morphology of Iron Oxide Nanoparticles with Reactive Concave Surfaces. A Compressed Sensing-Electron Tomography (CS-ET) Approach. Nano Lett., 11 (2011), 4666-4673. https://doi.org/10.1021/nl202253a.

[78] H. M. Gach, C. Tanase, F. Boada, 2D & 3D Shepp-Logan Phantom Standards for MRI, in ICSENG '08 Proceedings of the 2008 19th International Conference on Systems Engineering, August 19-21, 2008, IEEE Computer Society Washington, DC, USA, 2008, pp. 521–526. https://doi.org/10.1109/ICSEng.2008.15.

[79] T. Printemps, G. Mula, D. Sette, P. Bleuet, V. Delaye, N. Bernier, A. Grenier, G. Audoit, N. Gambacorti, L. Hervé, Self-adapting denoising, alignment and reconstruction in electron tomography in materials science. Ultramicroscopy, 160 (2016), 23-34. https://doi.org/10.1016/j.ultramic.2015.09.007.

[80] S. Li, L. Burel, C. Aquino, A. Tuel, F. Morfin, J.-L. Rousset, D. Farrusseng, Ultimate size control of encapsulated gold nanoparticles. Chem. Commun., 49 (2013), 8507-8509. https://doi.org/10.1039/C3CC44843F.

[81] ImageJ, https://imagej.nih.gov/ij/ (accessed July 14, 2017).

[82] A. Fedorov, R. Beichel, J. Kalpathy-Cramer, J. Finet, J.-C. Fillion-Robin, S. Pujol, C. Bauer, D. Jennings, F. Fennessy, M. Sonka, J. Buatti, S. Aylward, J. V. Miller, S. Pieper, R. Kikinis, 3D Slicer as an image computing platform for the Quantitative Imaging Network.Magn. Reson. Imaging, 30 (2012), 1323-1341. https://doi.org/10.1016/j.mri.2012.05.001.

[83] M. L. Derrien, Selective hydrogenation applied to the refining of petrochemical raw materials produced by steam cracking. Stud. Surf. Sci. Catal., 27 (1986), 613-666. https://doi.org/10.1016/S0167-2991(08)65364-1.

[84] T. Epicier, S. Koneti, P. Avenier, A. Cabiac, A.-S. Gay, L. Roiban, 2D & 3D in situ study of the calcination of Pd nanocatalysts supported on delta-Alumina in an Environmental Transmission Electron Microscope, Catalysis Today, available online 2019, January 29. https://doi.org/10.1016/j.cattod.2019.01.061.

[85] L. Gan, G. J. Jensen, Electron tomography of cells. Q. Rev. Biophys., 45 1 (2012), 27-56. https://doi.org/10.1017/S0033583511000102.

[86] R. Blakemore, Magnetotactic bacteria. Science, 190 (1975), 377-379. http://dx.doi.org/10.1126/science.170679.

[87] D. Faivre, D. Schüler, Magnetotactic bacteria and magnetosomes. Chem. Rev., 108 11 (2008), 4875-4898. https://doi.org/10.1021/cr078258w.

[88] C. T. Lefèvre, N. Menguy, F. Abreu, U. Lins, M. Pósfai, T. Prozorov, D. Pignol, R. B. Frankel, D. A. Bazylinski, A cultured greigite-producing magnetotactic bacterium in a novel group of sulfate-reducing bacteria. Science, 334 (2011), 1720-1723. https://doi.org/10.1126/science.1212596.

[89] J. P. Buban, Q. Ramasse, B. Gipson, N. D. Browning, H. Stahlberg, High-resolution low-dose scanning transmission electron microscopy. J. Electron Microsc. (Tokyo), 59 (2010), 103-112. https://doi.org/10.1093/jmicro/dfp052.

[90] L. F. Kourkoutis, J. M. Plitzko, W. Baumeister, Electron Microscopy of Biological Materials at the Nanometer Scale. Annu. Rev. Mater. Res., 42 (2012), 33-58. https://doi.org/10.1146/annurev-matsci-070511-155004.

[91] F. Dalmas, S. Pearson, B. Gary, J-M. Chenal, E. B-Lami, V. Prévot, L. Chazeau, Tailored microstructure and mechanical properties of nanocomposite films made from polyacrylic/LDH hybrid latexes synthesized by RAFT-mediated emulsion polymerization. Polym. Chem., 9 (2018), 2590-2600. https://doi.org/10.1039/C8PY00268A.

[92] H.-B. Hsueh, C.-Y. Chen, Preparation and properties of LDHs epoxy nanocomposites. Polymer, 44 (2003), 5275-5283. https://doi.org/10.1016/S0032-3861(03)00579-2.

[93] A. Das, F. R. Costa, U. Wagenknecht, G. Heinrich, Rubber composites based on silane-treated stöber silica and nitrile rubber Interaction of treated silica with rubber matrix. Eur. Polym. J., 44 (2008), 3456-3465. https://doi.org/10.1177/0095244313507807.

[94] M. C. Gastuche, G. Brown, M. M. Mortland, Mixed Magnesium-Aluminium Hydroxides. I. Preparation and characterization of compounds formed in dialysed systems. Clay Miner., 7 (1967), 177-192. https://doi.org/10.1180/claymin.1967.007.2.05.

[95] M. Bellotto, B. Rebours, O. Clause, J. Lynch, D. Bazin, E. Elka, A Reexamination of Hydrotalcite Crystal Chemistry. J. Phys. Chem., 100 (1996), 8527-8534. https://doi.org/10.1021/jp960039j.

[96] K. Masenelli-Varlot, C. Gauthier, L. Chazeau, F. Dalmas, T. Epicier, J.Y. Cavaillé, chap. 10 in Polymer Nanotube Nanocomposites, ed. V. Mittal (ed.), Scrivener Publishing, Beverly, MA, 2014, pp. 365-404. https://doi.org/10.10029781118945964.ch10.

[97] J. Martins, N. Batail, S. Silva, S. Rafik-Clement, A. Karelovic, D. P. Debecker, A. Chaumonnot, D. Uzio, CO_2 hydrogenation with shape-controlled Pd nanoparticles embedded in mesoporous silica: Elucidating stability and selectivity issues. Catal. Commun., 58 (2015), 11-15. http://dx.doi.org/10.1016/j.catcom.2014.08.027.

[98] H. Banjak, M. Costin, C. Vienne, R. Guillamet, V. Kaftandjian, Iterative CT reconstruction on limited angle trajectories applied to robotic inspection. AIP Conf. Proc., 1806 (2017), 020009. https://doi.org/10.1063/1.4974550.

[99] E. Y. Sidky, X. Pan, Image reconstruction in circular cone-beam computed tomography by constrained, total-variation minimization. Phys. Med. Biol., 53 (2008), 4777-4807. https://doi.org/10.1088/0031-9155/53/17/021.

[100] A. Beck, M. Teboulle, A Fast Iterative Shrinkage-Thresholding Algorithm for Linear Inverse Problems. SIAM J. Imaging Sci., 2 (2009), 183-202. https://doi.org/10.1137/080716542.

[101] Á. Molnár, A. Sárkány, M. Varga, Hydrogenation of carbon–carbon multiple bonds: chemo-, regio-and stereo-selectivity. J. Mol. Catal. Chem., 173 (2001), 185-221. https://doi.org/10.1016/S1381-1169(01)00150-9.

[102] Camstudio – Desktop Screen Recorder, https://camstudio.org/ (accessed February 05, 2019).

[103] A.J.Koster, A.Van den Bos, K.D.van der Mast, An autofocus method for a TEM. Ultramicroscopy 21 (1987) 209-222. https://doi.org/10.1016/0304-3991(87)90146-X.

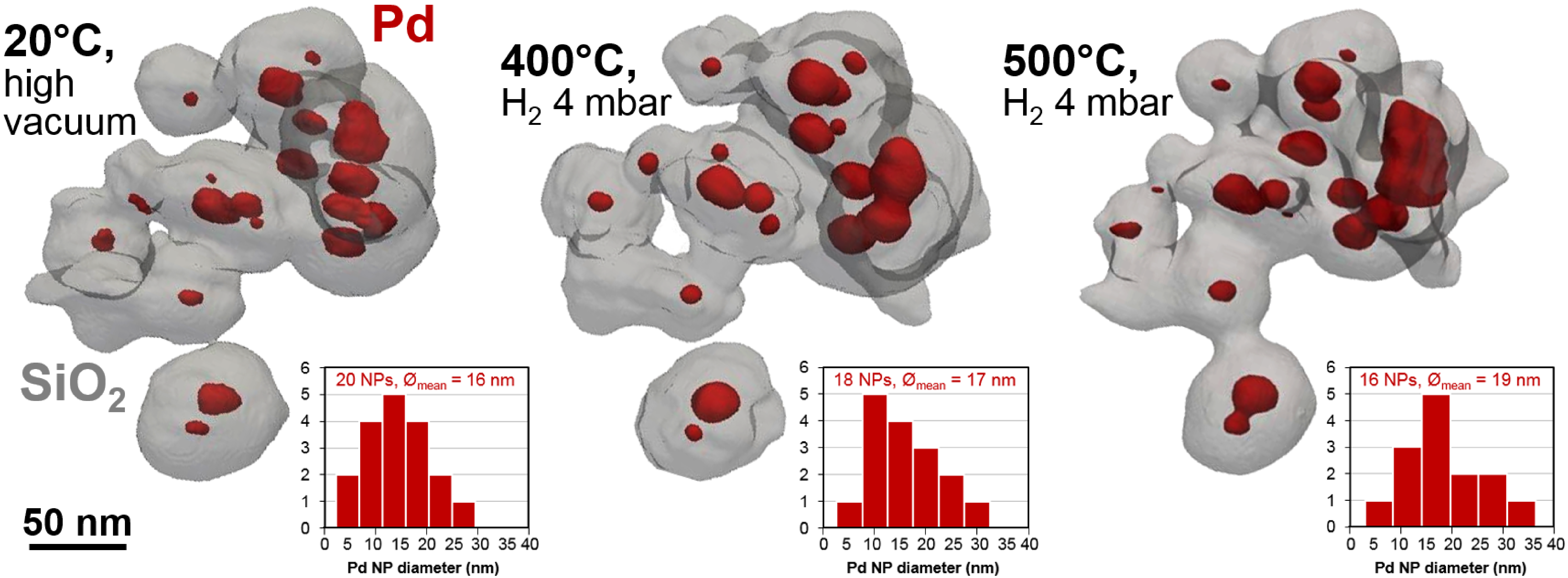
20°C,
high vacuum
Pd
SiO$_2$
50 nm
20 NPs, Ø$_{mean}$ = 16 nm
400°C,
H$_2$ 4 mbar
18 NPs, Ø$_{mean}$ = 17 nm
500°C,
H$_2$ 4 mbar
16 NPs, Ø$_{mean}$ = 19 nm
0 1 2 3 4 5 6
0 5 10 15 20 25 30 35 40
Pd NP diameter (nm)